Temperature field model for large spatial structures: Experiments, simulation and ANN prediction

Yiwen Wu [a, b, c], Shenggang Fan [a, b *], Minze Zhang [c], Leroy Gardner [c]

[a] Key Laboratory of Concrete and Prestressed Concrete Structures of Ministry of Education, Southeast University, Nanjing 211189, China

[b] School of Civil Engineering, Southeast University, Nanjing 211189, China

[c] Department of Civil and Environmental Engineering, Imperial College London, London SW7 2AZ, UK

* Corresponding author, E-mail address: 101010393@seu.edu.cn

Abstract: Large spatial stainless steel structures can be susceptible to accidental events such as fires, given their high occupancy, wide range of combustible materials and diverse usage. Consequently, a comprehensive investigation into the temperature field in large spatial stainless steel structures in the event of a fire has been conducted, encompassing experiments, simulations, assessments and predictions. Eight scaled temperature field tests were performed using a pool fire as the fire source, a common scenario in fire incidents. Building on the completed tests, a calibrated CFD model was developed using the Fire Dynamics Simulator (FDS) software and employed to further analyse the temperature field in large spatial structures under various fire powers and radii. A total of 8064 sets of three-dimensional large spatial temperature field data were acquired. Existing temperature field models, both from codes and other research studies, were evaluated against a substantial dataset. The results indicated that current models tend to be conservative, especially in areas near the fire source. In response to these findings, a novel approach utilizing Artificial Neural Networks to predict the 3D spatial temperature field in large spatial stainless steel structures is introduced. In addition, compared with the complex calculation formulae of traditional models, the model proposed herein based on

Artificial Neural Networks is more convenient to use in practice and exhibits better accuracy.

Keywords: FDS, Large spatial, Machine learning, Pool fire, Stainless steel, Temperature field.

Notations	
x_n	time-domain wave
X_k	frequency-domain wave
N	total number of samples
n	index of the time-domain sequence
k	independent variable
Q	heat release rate
ρ_0	ambient air density
c_p	specific heat of air at constant pressure
T_0	ambient air temperature
g	gravitational acceleration
α	fire growth coefficient
t	time
T	temperature of the centreline of the fire plume
z	height
k and η	coefficients of McCaffrey model
C_T	constant, typically set equal to 9.1
Q_c	convective part of the heat release rate
z_0	location of the virtual ignition source
H_f	average flame height
C_{Tf}	constant, typically set at 0.5
X_r	radiation factor
$\Delta h_c/s_a$	energy released per unit mass of air consumed by combustion reactions
y_j	output parameter
x_i	input parameter
g'	activation function
w_{ij}	weight coefficient
θ_j	bias
L	side length of the oil pan
A	oil pan area
y	horizontal distance from the fire source
a_i'	normalized value
a_i	original data
a	original data set
T_i	target value
O_i	output value
R^2	goodness of fit

MAE	mean absolute deviation
MSE	mean squared error

1. Introduction

Fire represents a significant natural hazard, presenting a substantial risk to human life and property [1]. The occurrence of fires is characterized by their suddenness, randomness and localized nature. Among these, building fires stand out as the most severe and direct threat to humanity. In recent years, as building functions have continuously improved and building decorations have become more luxurious, the fire load density in buildings has increased. This has led to a rise in the frequency of building fires, resulting in numerous casualties and significant economic losses [2].

The evolution of architectural design concepts has propelled the advancement of large spatial architecture. In contrast to traditional architecture, which primarily emphasizes formal aesthetics, large space architecture places a stronger focus on the functionality and efficiency of the structure. This evolving design concept reflects increasing demand for building functionality and sustainability. Throughout the development of large spatial structures, certain successful cases have emerged as noteworthy examples. The iconic Bird's Nest and London Olympic Stadium are showcased in **Fig. 1**. Large spatial structures often host significant events with a high density of people. Consequently, the occurrence of a fire could lead to immeasurable losses. Therefore, the study of fires in large spatial structures holds immense significance.



(a) Beijing Olympic Stadium (Bird's Nest) [3]



(b) London Olympic Stadium [4]

Fig. 1. Representative large spatial structures

Recent research [5, 6] has highlighted that applying traditional design methods to large spatial structures could yield results that are either overly conservative or unsafe. Consequently, the adoption of performance-based fire resistance design methods has been widely advocated [7]. In this approach, the fire behaviour of a building is analyzed considering its spatial and structural characteristics, along with the potential real fire scenarios it might encounter [8]. Furthermore, the temperature field of actual fire scenarios within large spaces are examined and integrated into the structural performance assessment [9].

Owing to smoke posing the primary threat to personal safety, current fire research on large spatial structures predominantly centres around smoke flow and control. Following a fire incident, the plume becomes the primary conduit for the transfer of mass and heat from the fire source to the external environment, forming the foundation for regional model development and the exploration of smoke movement patterns. Numerous theoretical and experimental investigations into plumes have been undertaken, presenting various plume models such as those proposed by Thomas et al. [10], McCafery [11], Zukoski et al. [12] and Heskestad [13, 14]. These studies have significantly advanced the understanding of smoke movement in building fires. Subsequently, further experimental research [15-19], numerical simulations [20-23] and theoretical analyses [24-31] have been conducted, contributing

to the refinement of the plume models. However, these studies have predominantly employed two-dimensional plume models that may not fully capture the temperature field in three-dimensional spaces. Moreover, at times, these models can be overly intricate, making practical application challenging.

In light of the above, eight fire tests in large spaces under natural fire conditions were carried out and are presented herein. A novel approach is employed to process the test data, aiming to derive the most reasonable and accurate test results. Leveraging the reliable experimental data, a comprehensive set of numerical simulations is presented using Fire Dynamics Simulator (FDS) software, resulting in a substantial amount of valuable data. These datasets are employed to evaluate the accuracy and effectiveness of current codes and plume models. Ultimately, through the application of machine learning methods, a new, more accurate and user-friendly 3D model for predicting the temperature field in large spaces is proposed.

2. Overview of the fire experiments

Based on the "Future Garden" project showcased at the 11th Jiangsu Horticultural Expo in Nanjing, eight scale tests were conducted to assess the fire performance of large spatial stainless steel structures under natural fire conditions [32]. Stainless steel is gaining increasing usage in structural applications owing to its favourable combination of mechanical properties, corrosion resistance and fire performance [33-37]. In the scale fire tests, four fire sources were strategically positioned beneath the structure, as illustrated in **Fig. 2**. The specific measuring points are indicated in **Fig. 3**, where Fires A1, A2, B1 and B2 represent the four fire sources, while measuring points A1 ~ A5 and B1 ~ B5 represent the air temperature measuring points when Fires A1 and A2, as well as Fires B1 and B2, are ignited, respectively.

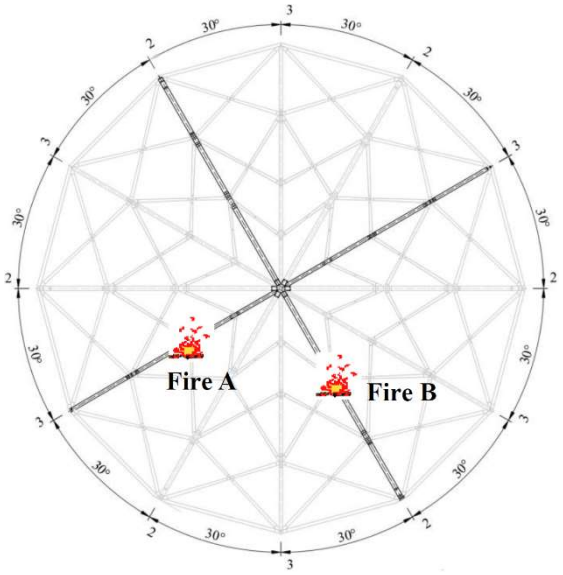

Fig. 2. Fire locations

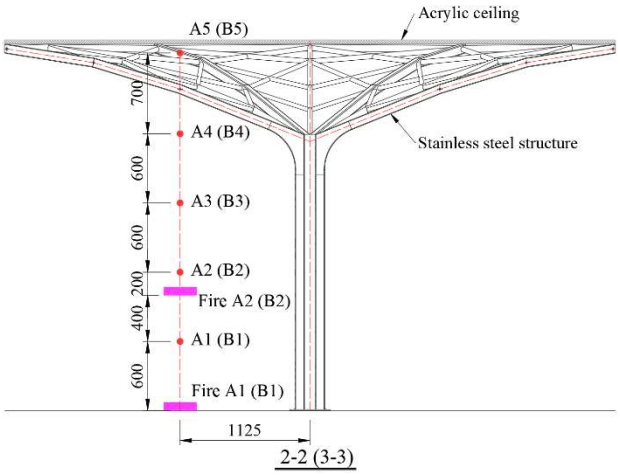

Fig. 3. Temperature measuring points (unit: mm)

To minimize the influence of the fire on the surrounding environment, a protective enclosure was installed using fire-resistant curtains, as depicted in **Fig. 4**. After the first four ignition tests were completed, they were repeated. Further details on the scale fire tests can be found in the comprehensive report by Wu et al [32].



Fig. 4. Fire test arrangement

3. Experimental results and data smoothing

During the on-site large space fire tests, the measured air temperature exhibited significant fluctuations, caused primarily by flame jumping and wind effects. These fluctuations made it challenging to assess the temperature of the measuring points directly. To address this issue, the Fourier

transform [38] was employed, along with other data processing techniques such as frequency statistics [39] and Kernel functions [40], to filter out the noise from the experimental data. This approach aimed to enhance the accuracy of the experimental results.

The Fourier transform is a powerful method for converting data from the time domain to the frequency domain, and has been widely used for the reduction of noise in signals. In the present application, high-frequency signals were first removed in the frequency domain to reduce noise. The processed frequency domain signal was then transformed back into a time domain signal through the inverse Fourier transform, yielding the denoised signal. **Eq. 1** describes the conversion of time-domain waves into frequency-domain waves, while **Eq. 2** describes the process of converting frequency-domain data back into time-domain waves after processing.

$$X_k = \sum_{n=0}^{N-1} x_n \cdot e^{-i2\pi kn/N} \tag{1}$$

$$x_n = \frac{1}{N} \sum_{k=0}^{N-1} X_k \cdot e^{i2\pi kn/N} \tag{2}$$

where x_n is the time-domain wave, X_k is the frequency-domain wave, N is the total number of samples, n is the index of the time-domain sequence and k is the independent variable.

After applying the Fourier transform, the originally erratic experimental curves were transformed into smoother curves. In this process, the minimum filtering noise frequency was set at 1 Hz, taking into account that, according to the on-site test videos, the frequency of flame jumping was approximately 2 Hz. Consequently, the Fourier transform fundamentally mitigated the influence of flame jumping. However, the fluctuation amplitude of the resulting test temperature curve remained substantial, posing challenges in pinpointing the specific standard temperature for each experiment.

In addition to the noise from flame jumping, the most impactful source of noise was identified as

wind on-site. However, the frequency of the wind was very low, making it challenging to filter through the Fourier transform. Instead, the epanechnikov Kernel distribution smoothing function in MATLAB [41] was used with all parameters set as default values.

Typical comparisons between the experimental data filtered through the Fourier transform and the Kernel function and the original measured data are illustrated in **Fig. 5**. All comparison results can be found in **Appendix I**. The effectiveness of the adopted filtering approach in removing the noise from the experimental data is clear.

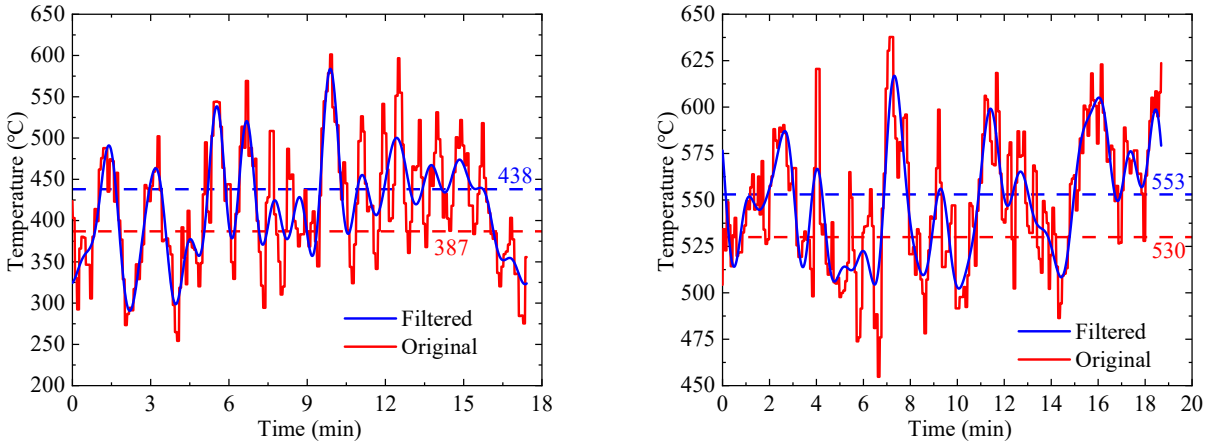

(a) Point A3 of Fire A2 in Test 1 (b) Point A3 of Fire A2 in Test 2

Fig. 5. Comparisons between the original and filtered experimental data

4. FDS simulation of large spatial temperature fields

The FDS software, developed by the National Institute of Standards and Technology (NIST) [42], simulates the propagation, combustion and smoke diffusion processes of fires. An FDS model is developed and validated against the described fire tests in this section. In Section 5, parametric studies are presented to explore the influence of fire power and oil pan size on the temperature field.

4.1 Establishment of geometric models

An FDS model of the fire tests was developed, as depicted in **Fig. 6**. To verify the accuracy of the FDS model, the model was established based on a 1:1 scale simulation of the experiments. The

mechanical properties of stainless steel and acrylic at elevated temperatures, as measured by Liu et al. [43] and Wu et al. [44], were utilized in the simulations. Gypsum boards were used to simulate the ground, as well as the platform supporting the fire source in cases where the fire sources were elevated.

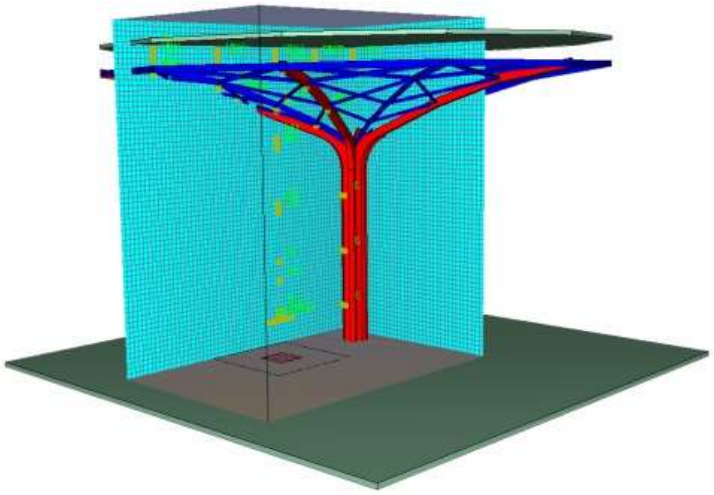

Fig. 6. FDS model of fire tests

4.2 Mesh generation and boundary conditions

Previous studies have indicated that FDS models typically utilize mesh sizes ranging from 1/16 to 1/4 of the characteristic diameter D^* of the fire source [22]. The characteristic diameter of the fire source D^* was calculated using **Eq. 3**. To meet the specific requirements of the FDS solver, the mesh number must be divisible by the product of any non-negative integer power of 2, 3 and 5. A mesh size of 0.05 m × 0.05 m × 0.05 m was adopted herein.

$$D^* = \left(\frac{Q}{\rho_0 c_p T_0 \sqrt{g}}\right)^{\frac{2}{5}} \tag{3}$$

where Q is the heat release rate, ρ_0 is the ambient air density, taken as 1.2754 kg/m^3, c_p is the specific heat of air at constant pressure, taken as 0.718 kJ/(kg·K), T_0 is the ambient air temperature, taken as 293 K and g is the gravitational acceleration, taken as 9.81 m/s^2.

In the experiments, despite the presence of an enclosure, there remained space around the structure itself, and the top was left open. Additionally, a 0.1 m gap was provided at the bottom, treating

it as an open space. In the FDS model, open boundaries were established around the model, excluding the ground, to align with the experiments and to ensure an adequate supply of oxygen.

4.3 Properties of fire sources

In the performance-based fire design of buildings, the initial incubation period of a fire, such as the smoldering stage, is typically disregarded, assuming that the fire begins with effective combustion. Consequently, the formula for the heat release rate is typically simplified to that shown in **Eq. 4**.

$$Q = \alpha t^2 \tag{4}$$

where Q is the heat release rate (kJ/s), α is the fire growth coefficient and t is the time (s).

In fire design scenarios, the heat release rates of different fire sources vary significantly. Research has found that the heat release rate of various fire sources is closely related to the square of time. Based on this, a fire growth model named the "t^2 fire" has been developed. The t^2 fire is further classified into four types based on different fire growth coefficients: slow, medium, fast and ultra-fast, as illustrated in **Fig. 7**, with respective fire growth coefficients of 0.002931, 0.01127, 0.04689, and 0.1878 [45]. For the simulations presented herein, the fire sources were consistent with the experiments, employing a pool fire with n-heptane as the fuel. The fire power matched the measured values in the experiments, and a t^2 fire was employed to define the initial ignition stage of the fire source. Since the fire source was a pool fire, it fell into the category of ultra-fast fires, with a fire growth coefficient of 0.1878.

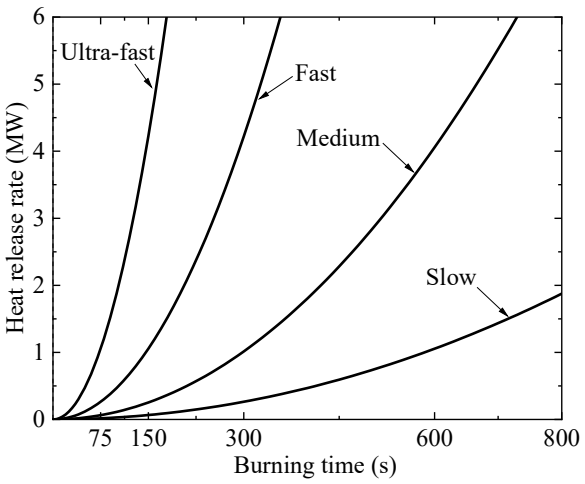

Fig. 7. Heat release rates of different types of t^2 fire

4.4 Validation of the FDS model

The air temperature simulated by the FDS model is compared with the original experimental data, as well as the data acquired after Fourier transform and Kernel function filtering, in **Fig. 8**. Although there are slight differences between some results obtained from the FDS simulation and the experimental results, most of the experimental data aligns well with the FDS model. For the measuring points in the highest temperature zone, the air temperature obtained by the FDS model is slightly higher. This discrepancy may arise because, during the experiments, some measuring points may deviate from the centreline of the fire due to the influence of gravity and wind, resulting in lower temperatures. This observation also implies, from another perspective, that the FDS model provides a certain level of conservation. For individual points with notable deviations, such as point A3 of Fire A2 in Test 1 and point B2 of Fire B1 in Test 2, upon post-experiment inspection, it was observed that the thermocouple at those measuring points had slid downwards along the fixed refractory steel wire. As the height increases, the difference between the predicted error of the model and the experiment becomes smaller and smaller. In addition, the heating trend in the initial stage of the experiment and FDS simulation is basically consistent, reflecting the reliability of FDS model. Except for a few measurement points with significant temperature fluctuations, the vast majority of measurement points have relatively stable

temperatures, which are consistent with FDS simulation. Overall, considering the challenges in controlling the experimental environment and various influencing factors in the fire test of an integrated structure in a large open space, it can be considered that the FDS model demonstrates good accuracy.

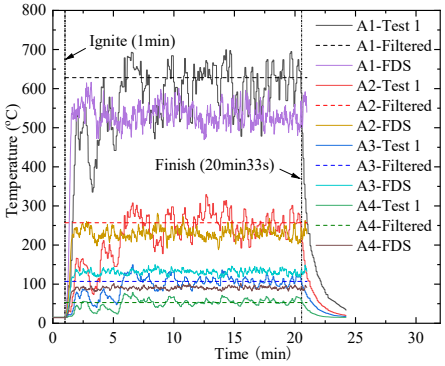

(a) Fire A1 – Test 1

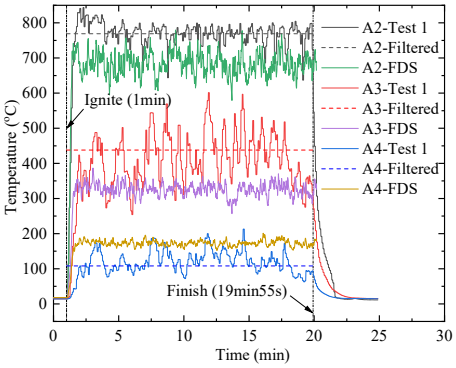

(b) Fire A2 – Test 1

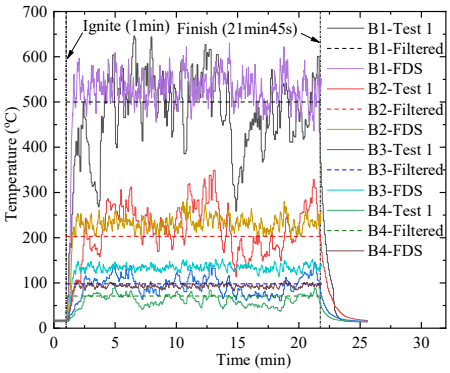

(c) Fire B1 – Test 1

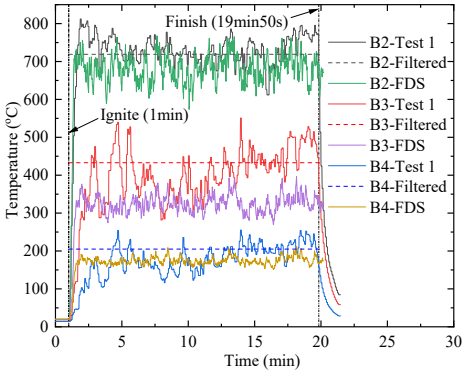

(d) Fire B2 – Test 1

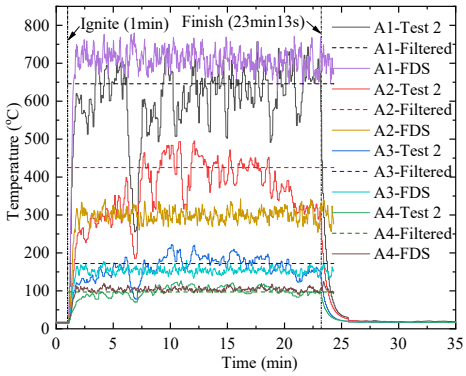

(e) Fire A1 – Test 2

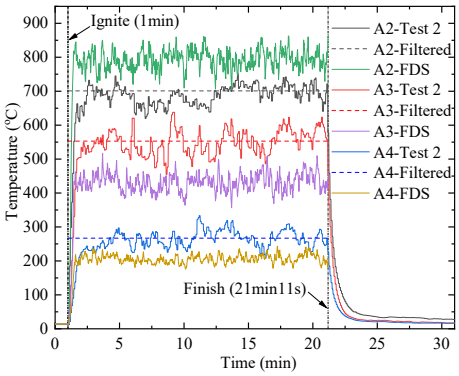

(f) Fire A2 – Test 2

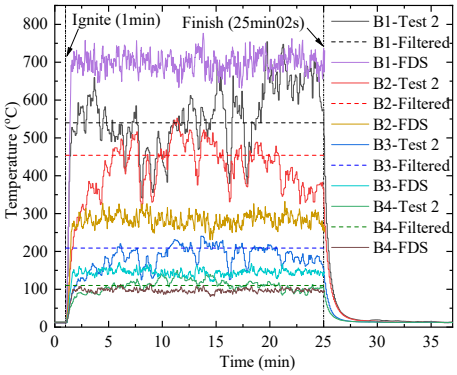

(g) Fire B1 – Test 2

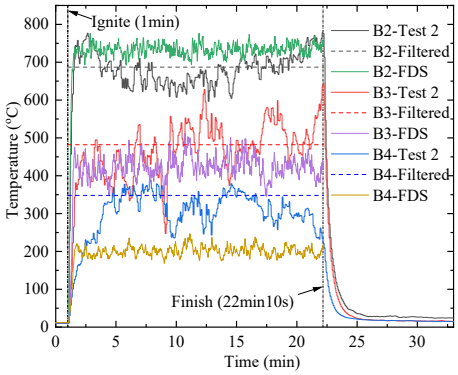

(h) Fire B2 – Test 2

Fig. 8. Comparisons of air temperature between FDS model and experimental data

176

177 # 5. Parametric analysis of large spatial temperature fields

178 Based on the validated FDS model in Section 4, further parametric analysis was conducted,
179 primarily exploring the effects of different fire powers and oil pan sizes (side lengths) on large spatial
180 temperature fields. Considering potential large space fire scenarios, the range of fire powers was set at
181 100 kW/m^2, 300 kW/m^2, 500 kW/m^2, 1 MW/m^2, 3 MW/m^2, 5 MW/m^2 and 10 MW/m^2. The range of
182 oil pan sizes (side length) was set at 0.5, 1, 1.5, 2, 3 and 5 m, resulting in a total of 42 FDS models. In
183 each model, the layout of the measuring points was kept constant. With the centre of the oil pan as the
184 origin, the height direction was arranged with measuring point positions at 0.5, 1, 2, 3, 4, 5, 6, 7, 8, 9,
185 10, 11, 12, 13, 14 and 15 m. The horizontal direction was arranged with measuring point positions at
186 0, 0.5, 1, 2, 3, 4, 5, 6, 7, 8, 9 and 10 m, resulting in a total of 192 measuring points for each fire source.
187 Owing to the symmetry of the simulated temperature field, spatial temperature data within a range of
188 15 m in height and 10 m in diameter around the fire source were determined from these 192 measuring
189 points, totaling 8064 data points.

190

191

6. Assessment of existing temperature field models

After combustible material ignites, flames and continuously rising hot smoke form above the ignition source, which is commonly referred to as a flame plume in fire combustion science. The fire plume can be divided into three regions, with the bottom being the continuous flame zone, the middle being the intermittent flame zone and the top being the smoke plume zone, as shown in **Fig. 9** [2]. Numerous studies into the spatial temperature field of pool fires have been carried out. This section summarizes several classical temperature field models and compares them with the data obtained from the experiments and FDS simulations to assess the accuracy of existing temperature field models.

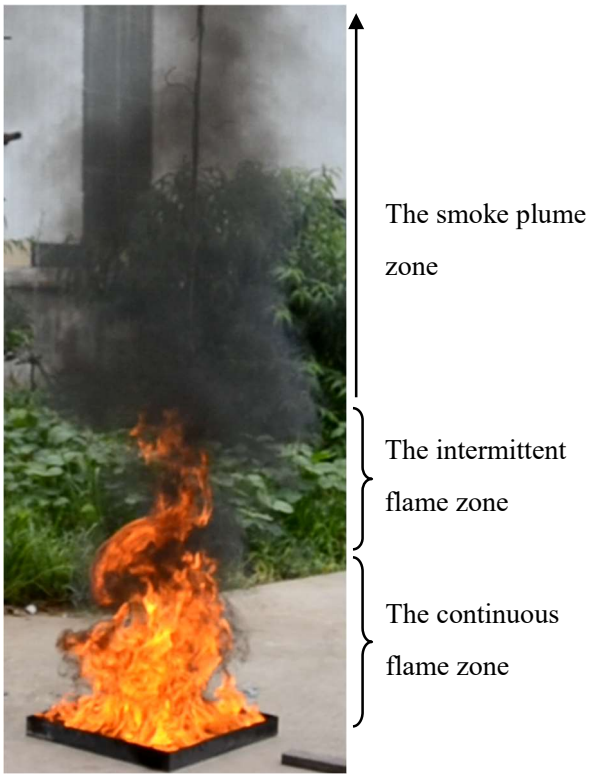

Fig. 9. A typical fire plume

6.1 Summary of existing models

The models proposed by McCaffrey [11], Zukoski et al. [12] and Heskestad [46] are presented in **Eqs. 5**, **6** and **7**, respectively.

$$T = (\frac{k}{0.9\sqrt{2g}})^2 (\frac{z}{Q^{2/5}})^{2\eta-1} T_0 + T_0 \quad (5)$$

$$T = 5(\frac{T_0}{g\rho_0^2 c_p^2})^{1/3} Q^{2/3} z^{-5/3} + T_0 \quad (6)$$

$$T = C_T (\frac{T_0}{g\rho_0^2 c_p^2})^{1/3} Q_c^{2/3} (z - z_0)^{-5/3} + T_0 \quad (7)$$

where T is the temperature of the centreline of the fire plume at height z, k and η are coefficients presented in **Table 1**, C_T is a constant, typically set equal to 9.1, Q_c is the convective part of the heat release rate, usually representing 60% to 80% of the total heat release rate and generally taken as $0.7Q$ and z_0 is the location of the virtual ignition source.

Table 1 Parameters of McCaffrey model

Zones	$z/Q^{2/5}$	η	k
Continuous flame zone	< 0.08	0.5	6.8
Intermittent flame zone	0.08 ~ 0.2	0	1.9
Plume zone	> 0.2	-1/3	1.1

The Zukoski et al. model [12] is specifically designed for the plume zone and is generally utilized for areas above the average flame height. The average flame height H_f is computed using **Eq. 8**.

$$H_f = 0.235Q^{2/5} - 1.02D^* \quad (8)$$

Heskestad [46] introduced the concept of virtual ignition sources and considered thermal radiation loss. The location of the virtual ignition source is determined by **Eq. 9**.

$$z_0 = 0.083Q^{2/5} - 1.02D^* \quad (9)$$

The Heskestad model is also suitable for areas above the flame height and has been incorporated into prEN 1991-1-2 [47] to calculate the temperature field for local fires, with a specified temperature not exceeding 900 ℃. For temperatures in the flame zone, when the fire source diameter does not exceed 1 m, the temperature can reach about 900 ℃. When the diameter exceeds 1 m, the temperature can reach up to 1200 ℃. Therefore, the flame zone temperature provisions in prEN l991-1-2 [47] and

McCaffrey [11] are applicable only to small fire sources with a diameter not exceeding 1 m. Ma and Quintiere [48] provided a calculation method for the flame zone temperature T, as shown in **Eq. 10**.

$$T = C_{T,f}(1 - X_r)\frac{\Delta h_c / s_a}{c_p} + T_0 \tag{10}$$

where $C_{T,f}$ is a constant, typically set at 0.5 and X_r is the radiation factor, which varies with the type and size of the fire source. For small fires with a diameter of no more than 1 m, X_r is generally set at 0.4, and for large fires with a diameter of more than 1 m, it is generally set at 0.2; $\Delta h_c/s_a$ is the energy released per unit mass of air consumed by combustion reactions and is generally set at 3000 kJ/kg.

6.2 Assessment of existing models

Comparisons between the experimental results and three considered existing models are illustrated in **Fig. 10**. From **Fig. 10**, at low heights, that is, close to the fire source, the predicted results from the existing models have a large deviation and tend to overestimate the air temperature at that location. As the height increases, the predicted results of the existing temperature field models become more accurate. This is because the impact of fire source shaking decreases with increasing distance, and the temperature remains similar over a larger range. Overall, the existing models cannot accurately reflect the air temperature along the centreline of the fire source during an actual fire.

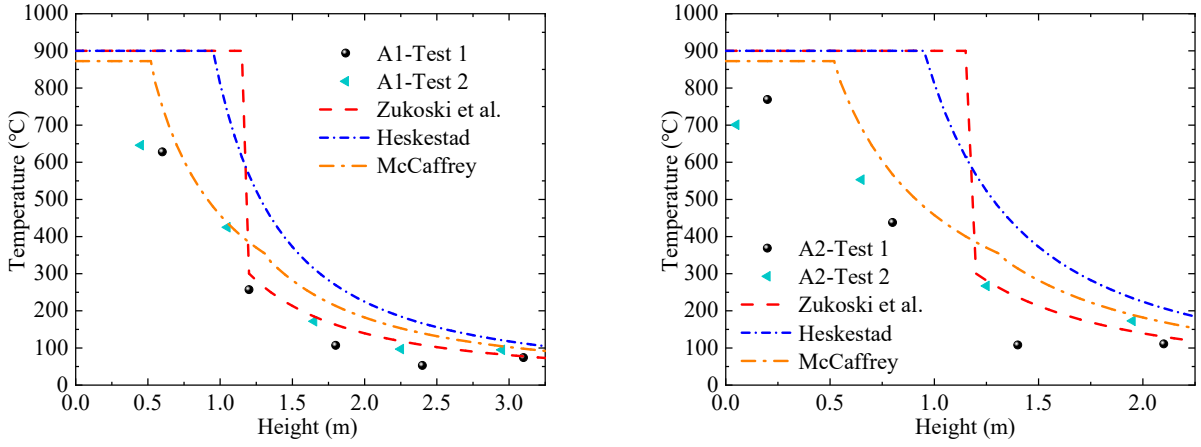

(a) Fire A1 (b) Fire A2

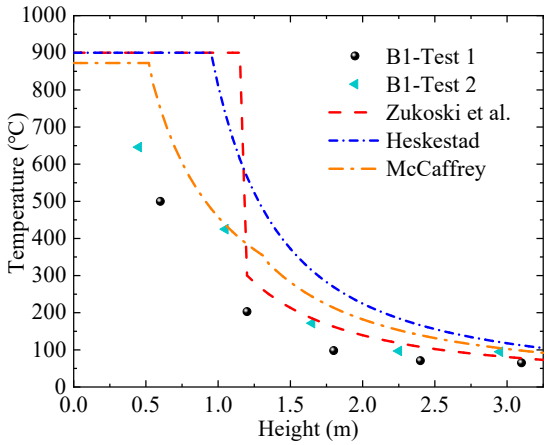

(c) Fire B1

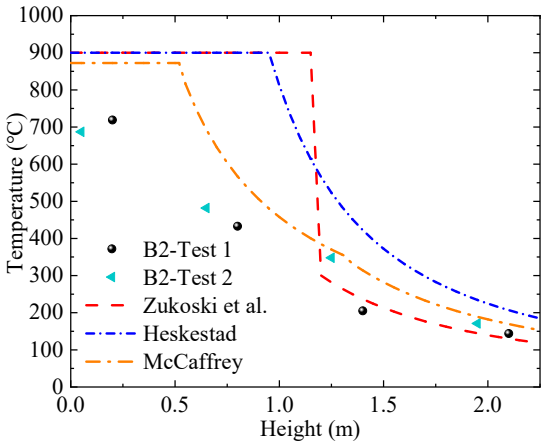

(d) Fire B2

Fig. 10. Comparisons of air temperature between existing models and experimental data

Comparisons between the results of the FDS simulations and existing models are shown in **Fig. 11** for two fire scenarios with a pan side length of 1.5 m. All comparison results can be found in **Appendix II**. From **Fig. 11**, when the fire power is less than 1 MW/m^2 and the height is greater than 6 m, the predicted results by the three models are accurate. The prediction errors increase with increasing oil pan side length and fire power. When the height is less than 3 m, the prediction errors significantly increase with the existing models tending to overestimate the temperature of the pool fires. In **Figs. 11(e)** to **11(g)**, when the height is less than 3 m, the air temperature of FDS simulation increases first and then decreases, which is different from that of fire power less than 3 MW/m^2. The main reason is that the height of the first measuring point in the FDS simulation is 0.5 m, and the maximum air temperature above the centre of the fire source increases with increasing of the fire power. When the fire power is small, the simulation cannot capture the characteristic point.

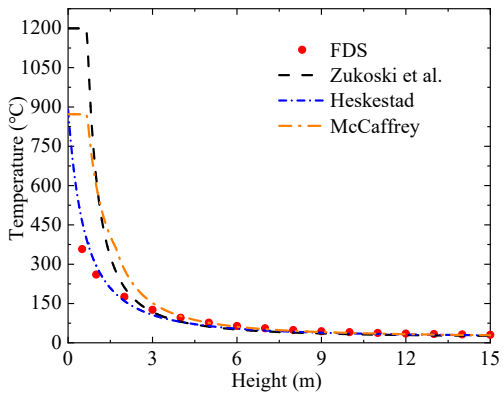

(a) 100 kW/m^2

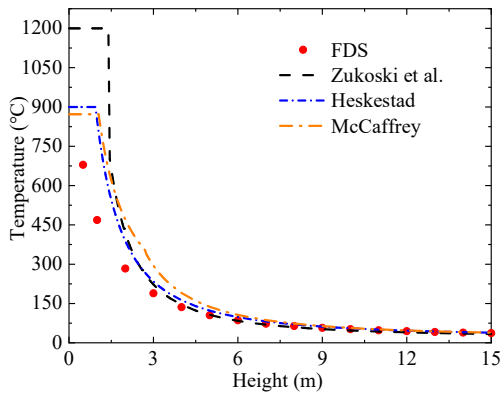

(b) 300 kW/m^2

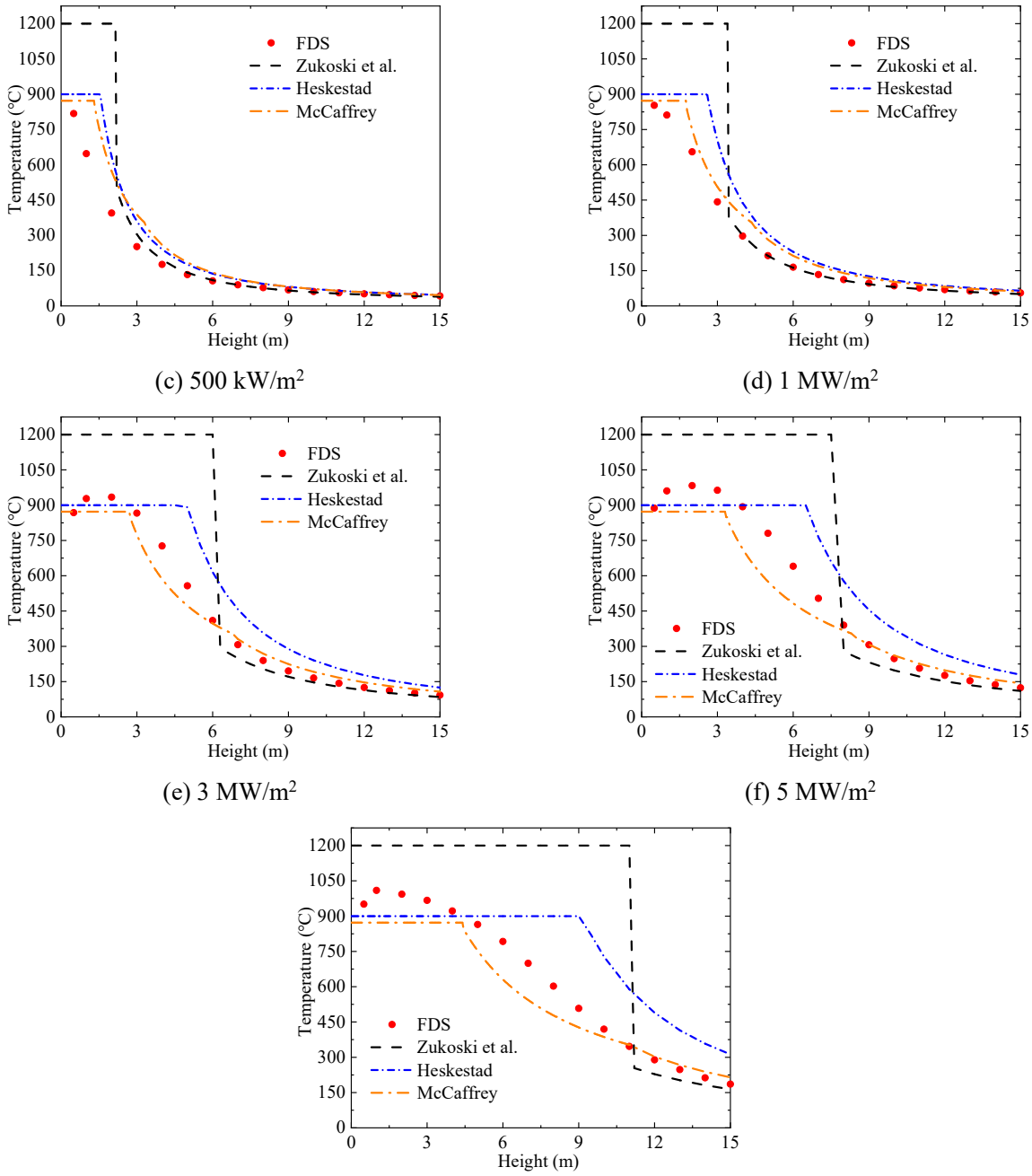

(c) 500 kW/m^2 (d) 1 MW/m^2

(e) 3 MW/m^2 (f) 5 MW/m^2

(g) 10 MW/m^2

Fig. 11. Comparisons of air temperature between the FDS simulations and existing models

242

243 7. A new temperature field model based on machine learning

244 In this section, Feedforward Multilayer Perceptron (MLP) models are employed to predict the
245 three-dimensional temperature field under different fire powers and fire source diameters. These
246 Artificial Neural Network (ANN) models consist of multiple layers strictly organized in one direction

(input layer, single or multiple hidden layers and output layer), each of which represents an interconnected 'neuron' system (or node). **Fig. 12** describes the composition of a typical MLP ANN neuron. In **Fig. 12**, the links formed between consecutive neurons are assigned specific weights, which are multiplied by the input values generated by the neurons. Subsequently, the values obtained from all neurons in a specific layer are transmitted through a link, added to the bias, and then introduced into a predefined activation function that represents the relationship between layers, as shown in **Eq. 11** [49]. The activation function is typically a sigmoid function, a hyperbolic tangent function or a linear function.

$$y_j = g_j^{'} = g^{'}(\sum_{i=1}^{i} w_{ij} x_i + \theta_j) \tag{11}$$

where y_j is the output parameter, x_i is the input parameter, $g^{'}$ is the activation function, w_{ij} is the weight coefficient and θ_j is the bias.

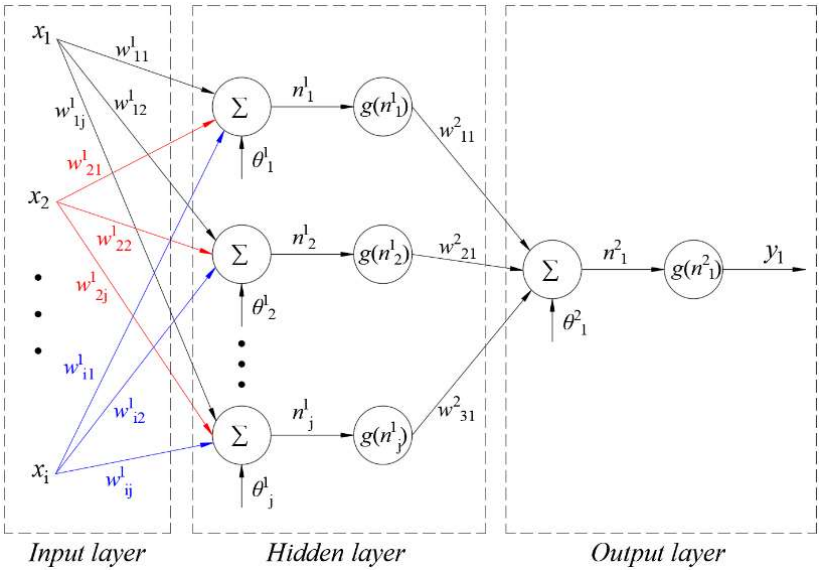

Fig. 12. A typical MLP ANN neuron

7.1 Input and output (target) parameters

Before conducting data input, it is necessary to determine the correlation between the parameters, and the smaller the correlation between the parameters, the better. The reasons are as follows: to reduce

redundant information, to accelerate the optimization process, to improve generalization performance and to avoid overfitting. The input parameters and output (target) parameters were obtained from the FDS simulations introduced above, with a total of 8064 samples. Correlation coefficient analysis was performed on these 8064 samples. In the preliminary analysis, the values not only included the relevant variables in the FDS simulations but also included the parameters the appeared in the existing theoretical formulae. The correlation coefficients between each parameter are shown in **Table 2**.

Table 2 Correlation coefficients between input parameters and output parameters

Coefficient	Q	Q'	L	D^*	A	y	z	T
Q	1.00	0.52	0.00	0.00	0.00	0.00	0.00	0.33
Q'	0.52	1.00	0.54	0.54	0.55	0.00	0.00	0.45
L	0.00	0.54	1.00	1.00	0.97	0.00	0.00	0.30
D^*	0.00	0.54	1.00	1.00	0.97	0.00	0.00	0.30
A	0.00	0.55	0.97	0.97	1.00	0.00	0.00	0.29
y	0.00	0.00	0.00	0.00	0.00	1.00	0.00	-0.46
z	0.00	0.00	0.00	0.00	0.00	0.00	1.00	-0.16
T	0.33	0.45	0.30	0.30	0.29	-0.46	-0.16	1.00

Note: L is the side length of the oil pan; A is the oil pan area; y is the horizontal distance from the fire source; z is the height.

When the correlation coefficient is greater than 0.7, it is considered to be a strong correlation, while a coefficient less than 0.5 indicates no strong correlation between the two parameters. In this study, to simplify the model and enhance usability for engineers, a rigorous screening process was applied to the parameters, ensuring minimal linear correlation. Additionally, the smaller the correlation between the input parameters, the better the simplicity, stability and generalization ability of the model. Therefore, only parameters with correlations close to 0 were retained. The final range and units of the retained input parameters and output (target) parameters are shown in **Table 3**.

Table 3 Range and units of selected input parameters and output parameters

Parameters	Q	R	y	z	T
Unit	kW/m^2	m	m	m	℃
Minimum	100	0.282	0	0.5	20.0
Maximum	10000	2.82	10	15	1141.5

To minimize numerical instability and enhance the rate of convergence, **Eq. 12** is used to normalize the values of the input and output (target) parameters within the range of [0,1].

$$a_i^{'} = \frac{a_i - \min(a)}{\max(a) - \min(a)} \tag{12}$$

where $a_i^{'}$ is the normalized value, a_i is the original data and a is the original data set.

7.2 ANN program architecture

The number of neurons in the input layer is determined by the number of parameters considered to have a significant impact on the temperature field, namely the five parameters listed in Table 4. The selection of the number of neurons in the hidden layer is usually in accordance with the results of parametric research. Since the research topic explored in this section has not yet been examined using the ANN method, a series of parametric studies were conducted on the number of hidden layers and the size of each layer. Through repeated calculations, it was found that using a 2-layer, 10 size hidden layer architecture resulted in the smallest training error.

7.3 Training, validation and testing of ANN models

The process of training a neural network involves adjusting the weights and bias values of the network, initially randomly assigned, to optimize network performance through an iterative process. The default performance function of a feedforward network is the mean squared error (MSE), which calculates the mean squared error between network outputs and is expressed by **Eq. 13**.

$$MSE = \frac{1}{N}\sum_{i=1}^{N}(T_i - O_i)^2 \tag{13}$$

where MSE is the mean squared error, T_i is the target value and O_i is the output value.

The error of each output node was calculated based on the difference between the calculated output and the expected output (target). To minimize the error obtained in each iteration, such that the

output value of the ANN was consistent with the target value, a backpropagation algorithm (or Delta rule) was utilized. To enhance the performance and accuracy of the ANN predictions, the normalized data (input and target values) were initially randomly divided into three subsets for training, validation and testing purposes. In this study, the data were first randomly arranged, with 20% of the data reserved for testing and the remaining 80% used for training and validation. Within the remaining 80% of the data, 70% was allocated for training and the remaining 30% was dedicated to validation. To summarize, 56% of the total data was used for training, 24% for validation and the remaining 20% for testing.

7.4 Accuracy verification of the ANN model

Comparisons between the predicted temperatures from the ANN model established in this study, the target temperatures and the experimental temperatures are illustrated in **Fig. 13**, where R^2 represents Goodness of Fit, *MAE* denotes Mean Absolute Deviation, and *MSE* stands for Mean-square Error. The uniform distribution of data points on both sides of the straight line, along with a R^2 approaching 1, clearly demonstrate the accuracy and applicability of the ANN model developed herein. The developed model offers engineers an accurate and practical means of predicting temperature fields in large spatial fires.

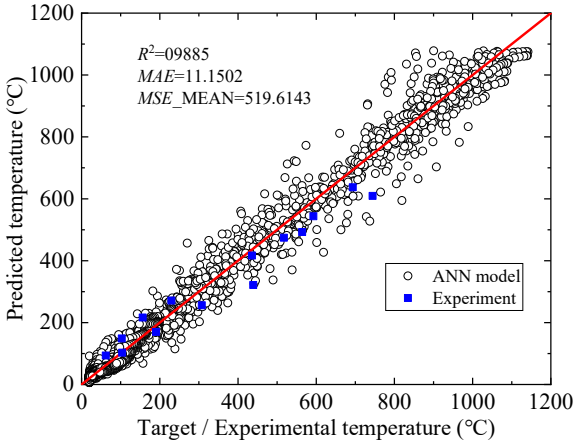

Fig. 13. Accuracy verification of the ANN model

Although current ANN models have achieved high accuracy, there are still some methods, such

as hyperparameter tuning, regularization techniques, data augmentation and synthetic data generation, transfer learning, advanced optimization algorithms, ensemble learning and dimensionality reduction, that can be used to further improve them. These temperature field analyses can be used to provide potential long-term structural implications such as material degradation, creep and thermal expansion, fatigue accumulation, corrosion acceleration and structural connections. In the future, several promising directions including material performance under extreme conditions, advanced fire-resistant materials, machine learning integration, structural resilience assessment, real-time monitoring and digital twins can be explored based on this study.

8. Conclusions

This study considers the analysis of temperature field models in large spaces based on scale fire tests. A series of large spatial fire tests was first described. An FDS model was then created to simulate the temperature field in large spatial fires and a parametric analysis was performed. Drawing insights from extensive experimental and simulation data, classical plume models were evaluated and a new three-dimensional large space temperature field model utilising machine learning methods was introduced. The construction details of the FDS and ANN models have been provided as well as the experimental results for verification, which can be used to conduct further analyses and design. The key findings are as follows:

(1) Utilizing the Fourier transform and the Kernel function, noise filtering was applied to the spatial temperature fields obtained from the experiments, yielding more reasonable and accurate spatial temperature field data;

(2) A parametric analysis was carried out using a validated FDS model, primarily investigating the

impacts of different fire source sizes and powers on the large space temperature field. A total of 8064 sets of three-dimensional large spatial temperature field data were acquired;

(3) Existing classical centreline plume models were evaluated using the experimental and parametric numerical data. At heights of less than 3 m, the prediction error of existing models significantly increases, and the predicted results of existing models are larger than those obtained from the tests and simulations. In general, the temperature of pool fires is overestimated by existing models;

(4) A new three-dimensional large space temperature field ANN model was proposed, based on the experimental and parametric data. Compared to the traditional centreline plume models, the new model was three-dimensional rather than two-dimensional, significantly simplifying the application process. The ANN model provides more accurate prediction results and offers engineers a more convenient and efficient prediction method. Furthermore, it aligns more closely with the current trend of performance-based fire resistance research and design.

Acknowledgments

The authors gratefully acknowledge the financial support of the National Natural Science Foundation of China (No. 52278153).

Appendix I. Comparisons between the original and filtered experimental data

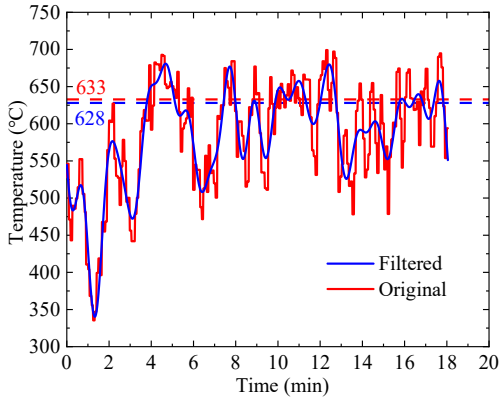

(a) Point A1 of Fire A1 in Test 1

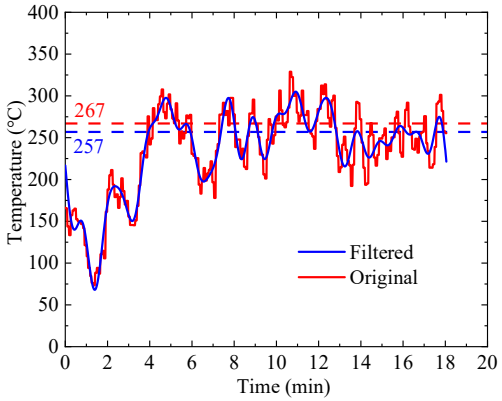

(b) Point A2 of Fire A1 in Test 1

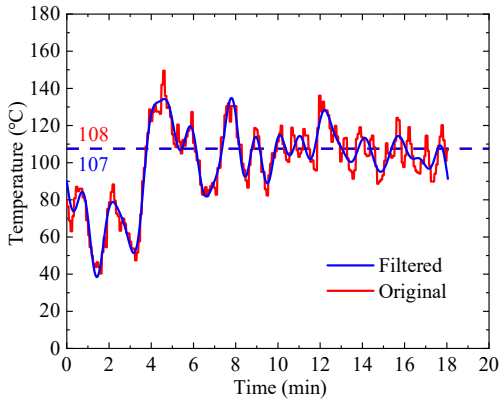

(c) Point A3 of Fire A1 in Test 1

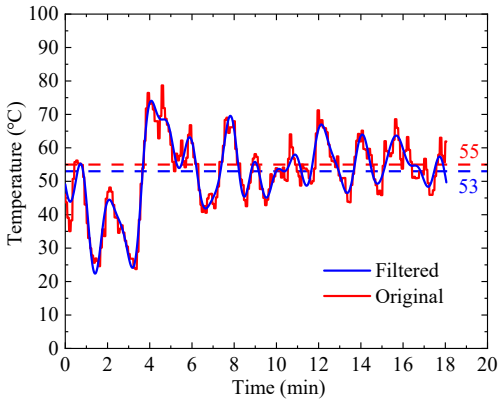

(d) Point A4 of Fire A1 in Test 1

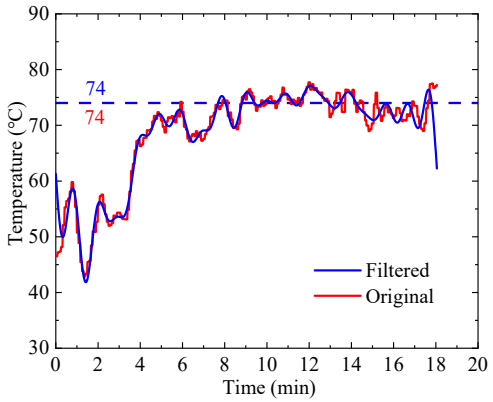

(e) Point A5 of Fire A1 in Test 1

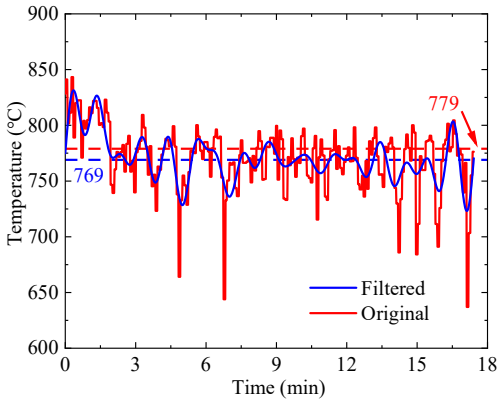

(f) Point A2 of Fire A2 in Test 1

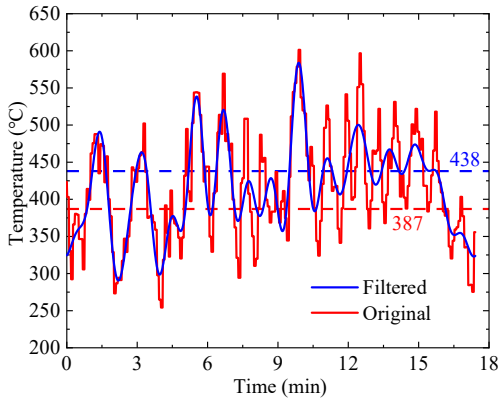

(g) Point A3 of Fire A2 in Test 1

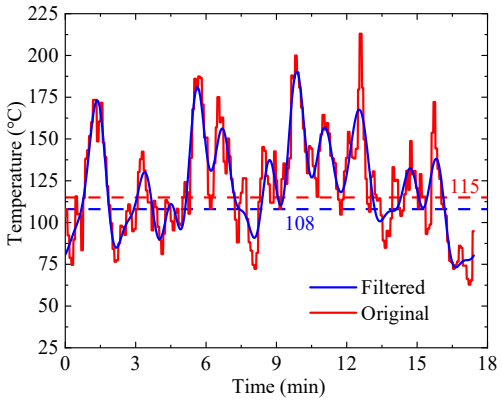

(h) Point A4 of Fire A2 in Test 1

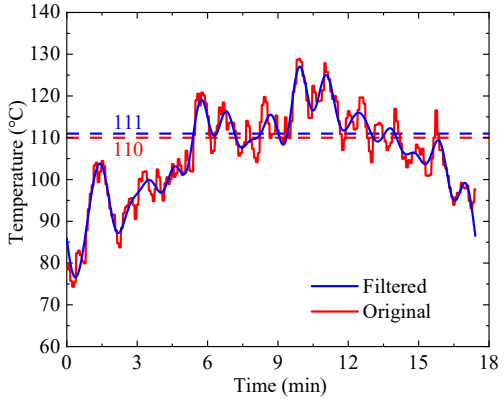

(i) Point A5 of Fire A2 in Test 1

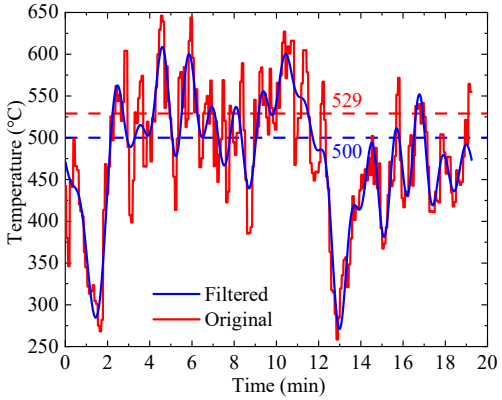

(j) Point B1 of Fire B1 in Test 1

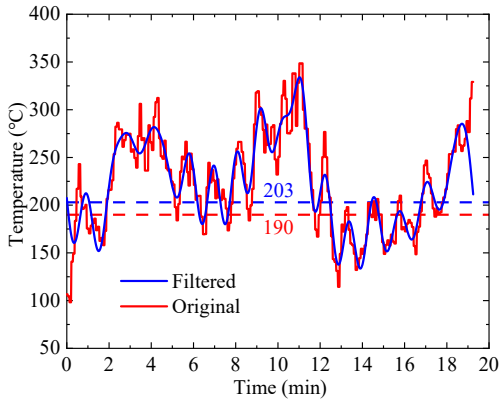

(k) Point B2 of Fire B1 in Test 1

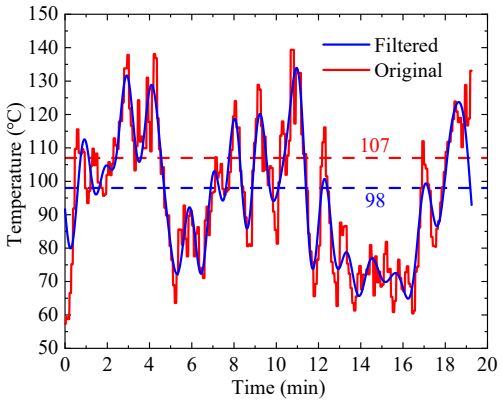

(l) Point B3 of Fire B1 in Test 1

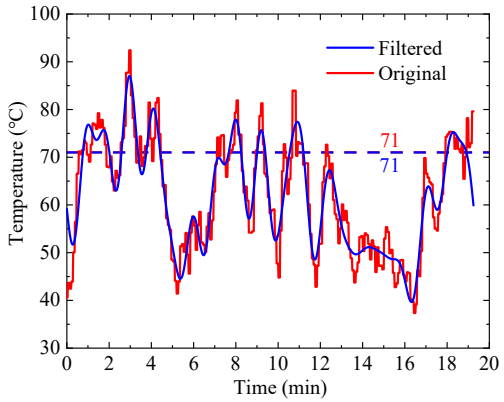

(m) Point B4 of Fire B1 in Test 1

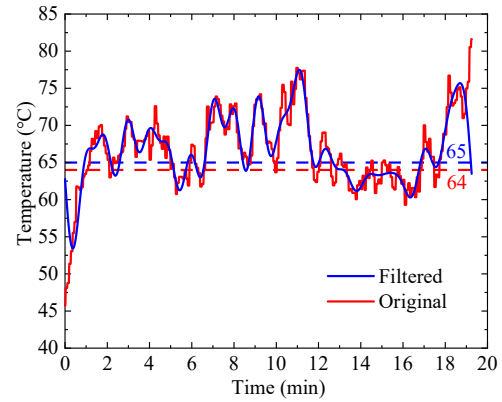

(n) Point B5 of Fire B1 in Test 1

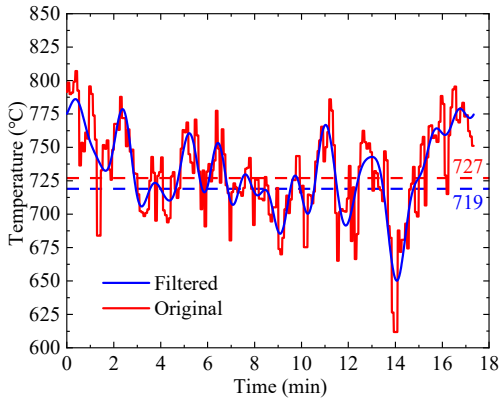

(o) Point B2 of Fire B2 in Test 1

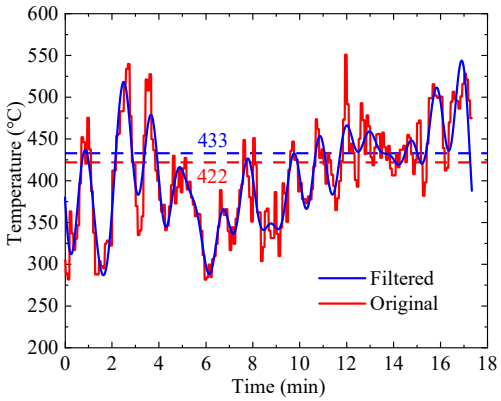

(p) Point B3 of Fire B2 in Test 1

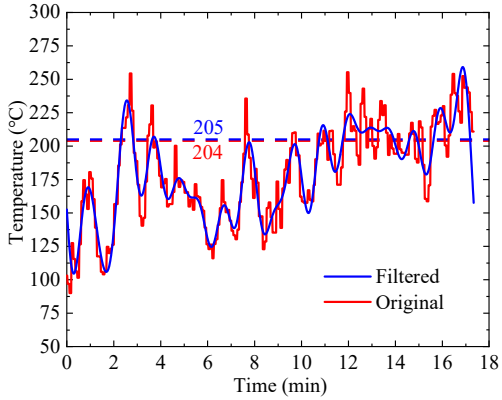

(q) Point B4 of Fire B2 in Test 1

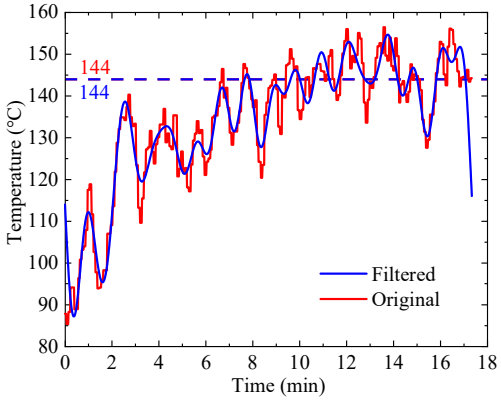

(r) Point B5 of Fire B2 in Test 1

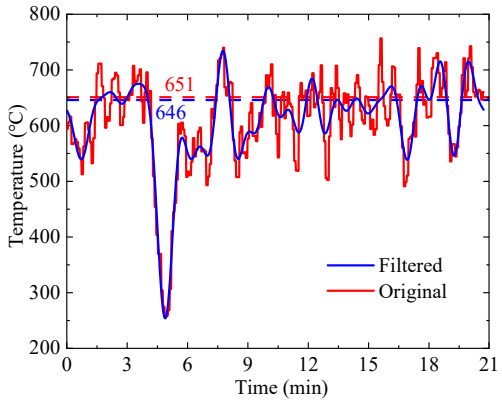

(s) Point A1 of Fire A1 in Test 2

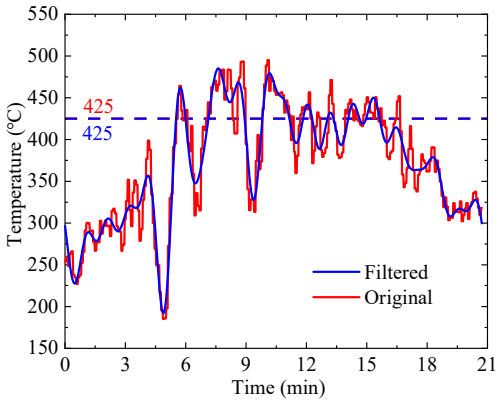

(t) Point A2 of Fire A1 in Test 2

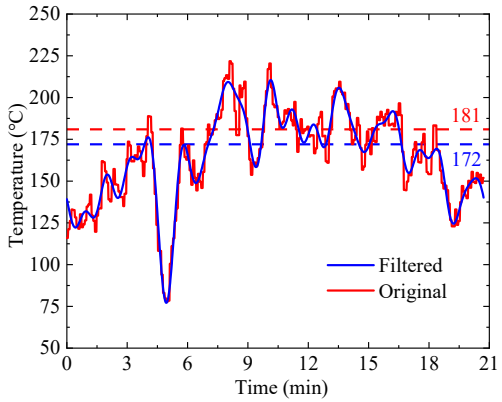

(u) Point A3 of Fire A1 in Test 2

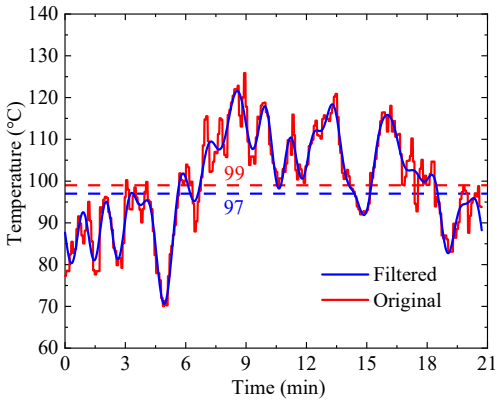

(v) Point A4 of Fire A1 in Test 2

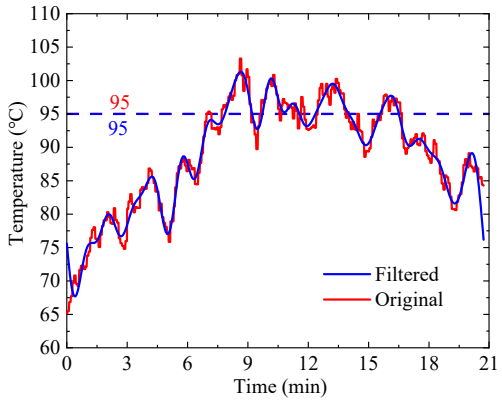

(w) Point A5 of Fire A1 in Test 2

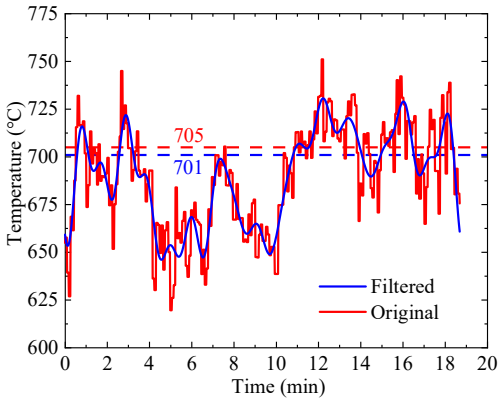

(x) Point A2 of Fire A2 in Test 2

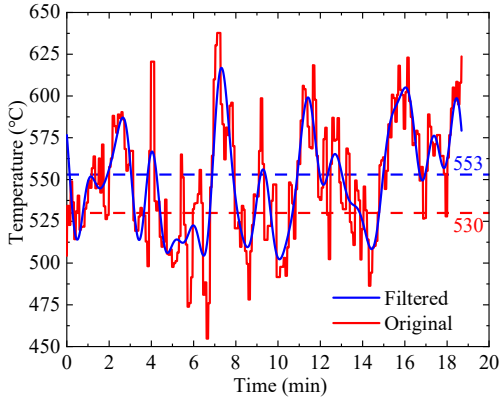

(y) Point A3 of Fire A2 in Test 2

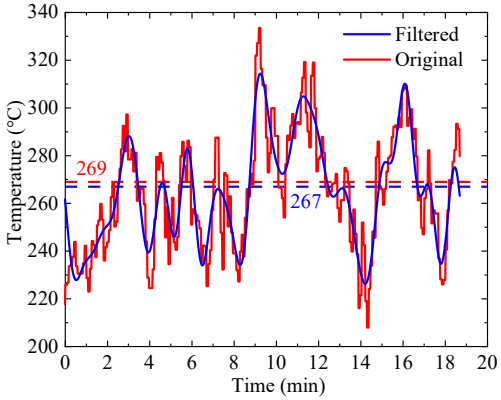

(z) Point A4 of Fire A2 in Test 2

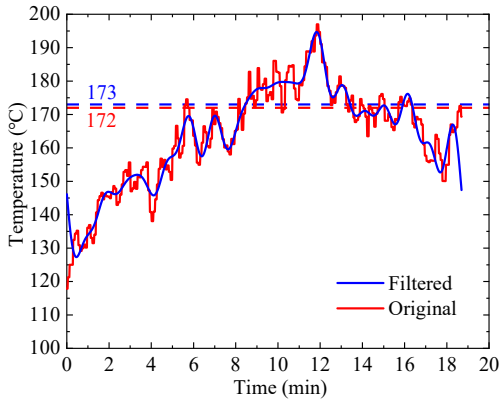

(aa) Point A5 of Fire A2 in Test 2

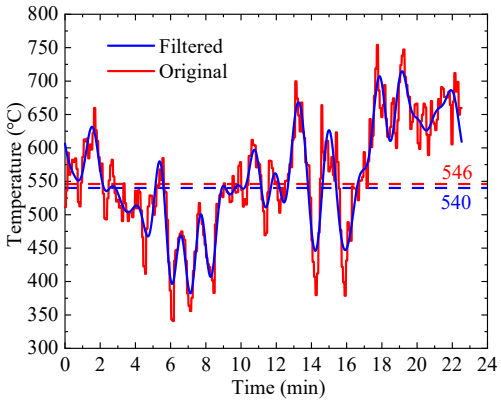

(ab) Point B1 of Fire B1 in Test 2

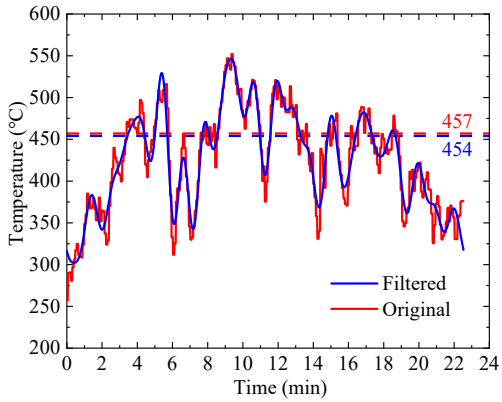

(ac) Point B2 of Fire B1 in Test 2

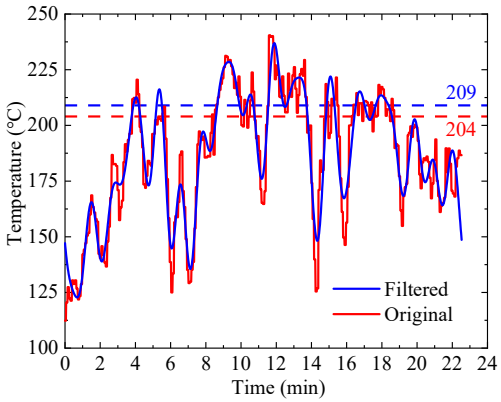

(ad) Point B3 of Fire B1 in Test 2

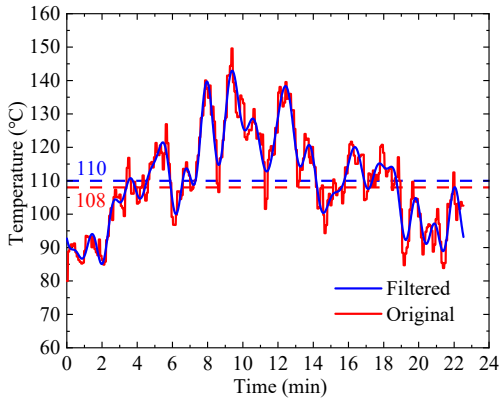

(ae) Point B4 of Fire B1 in Test 2

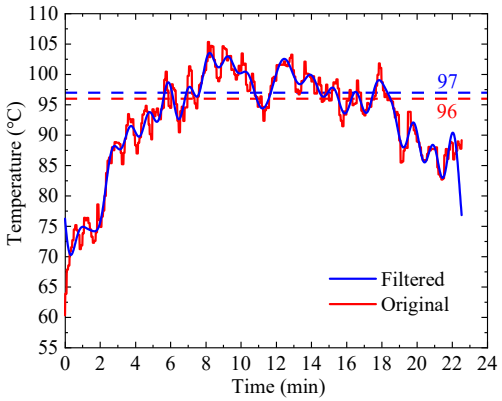

(af) Point B5 of Fire B1 in Test 2

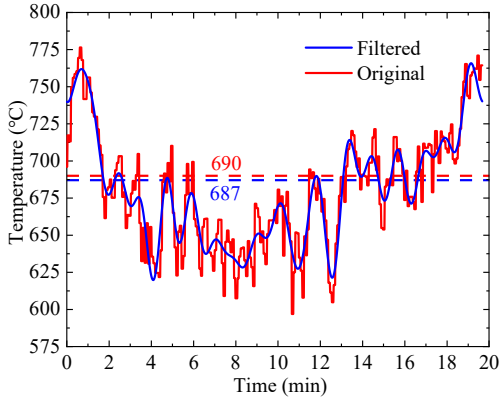

(ag) Point B2 of Fire B2 in Test 2

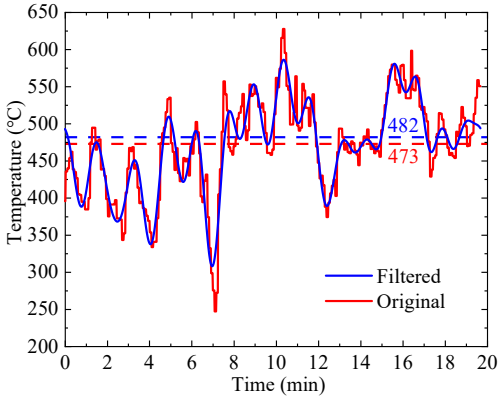

(ah) Point B3 of Fire B2 in Test 2

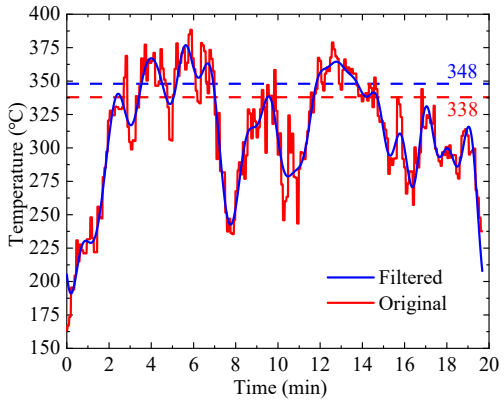

(ai) Point B4 of Fire B2 in Test 2

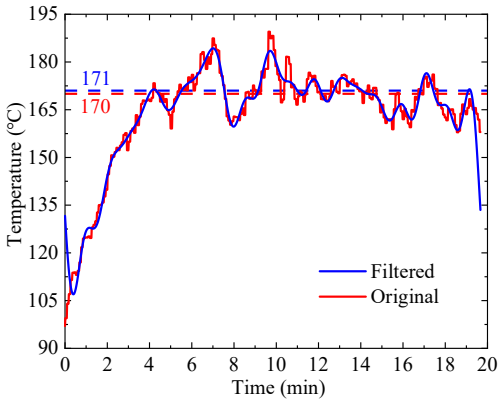

(aj) Point B5 of Fire B2 in Test 2

356

357

358

359

360

Appendix II. Comparisons of air temperature between the FDS simulations and existing models

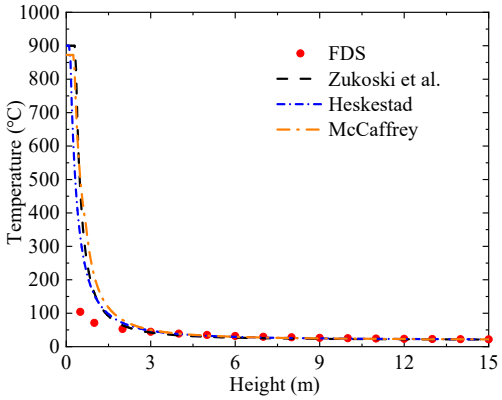

(a) Side length of 0.5 m – fire power of 100 kW/m^2

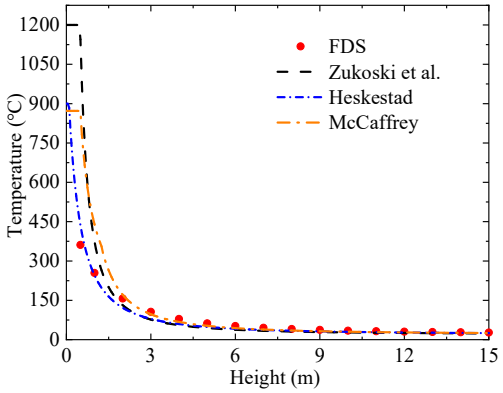

(b) Side length of 1 m – fire power of 100 kW/m^2

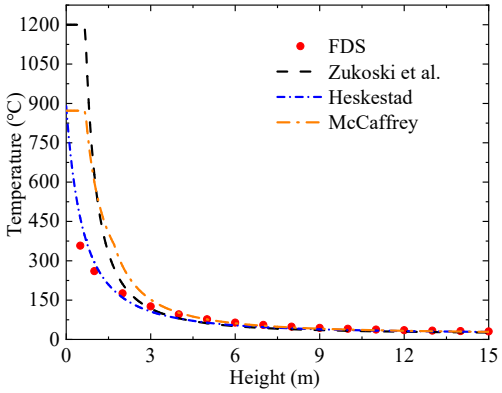

(c) Side length of 1.5 m – fire power of 100 kW/m^2

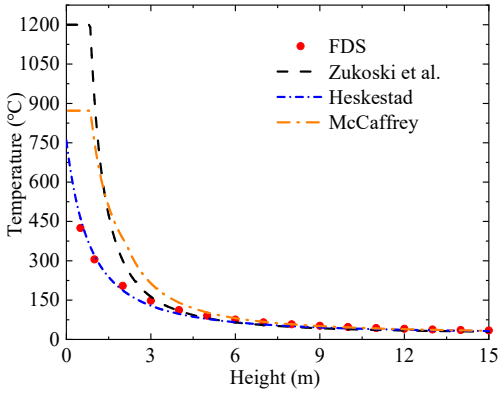

(d) Side length of 2 m – fire power of 100 kW/m^2

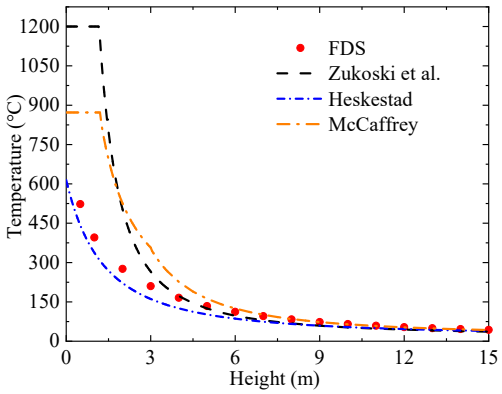

(e) Side length of 3 m – fire power of 100 kW/m^2

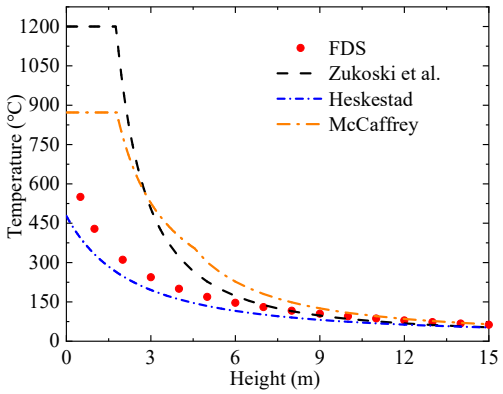

(f) Side length of 5 m – fire power of 100 kW/m^2

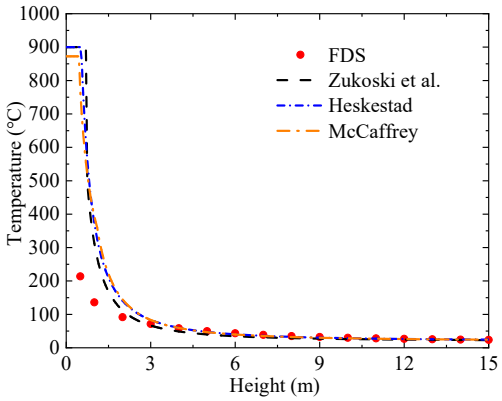

(g) Side length of 0.5 m – fire power of 300 kW/m^2

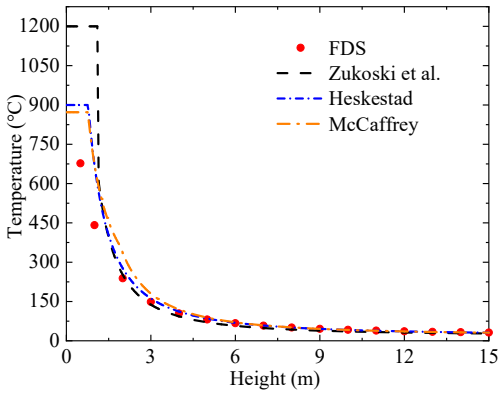

(h) Side length of 1 m – fire power of 300 kW/m^2

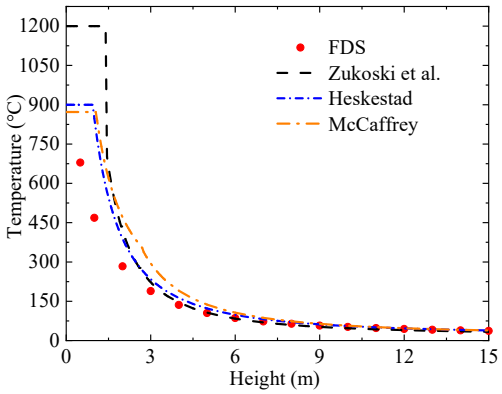

(i) Side length of 1.5 m – fire power of 300 kW/m^2

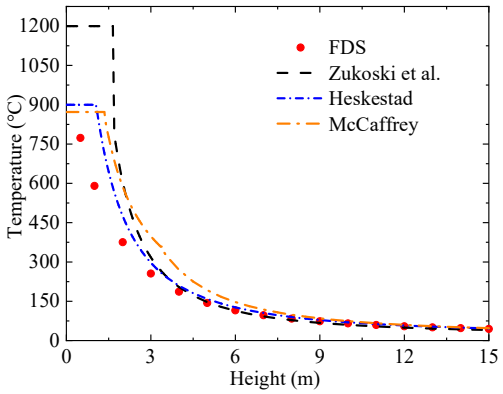

(j) Side length of 2 m – fire power of 300 kW/m^2

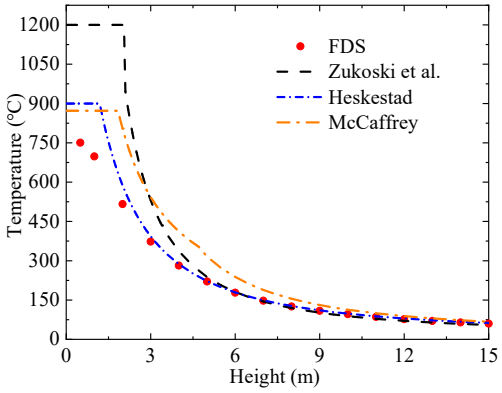

(k) Side length of 3 m – fire power of 300 kW/m^2

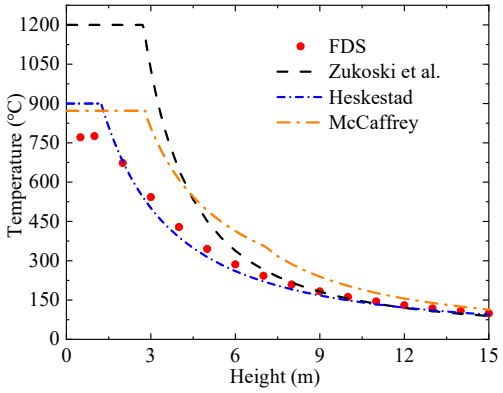

(l) Side length of 5 m – fire power of 300 kW/m^2

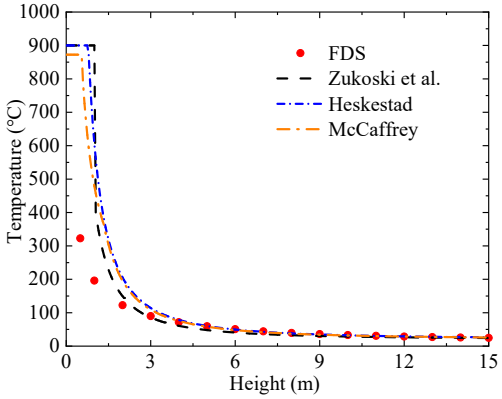

(m) Side length of 0.5 m – fire power of 500 kW/m^2

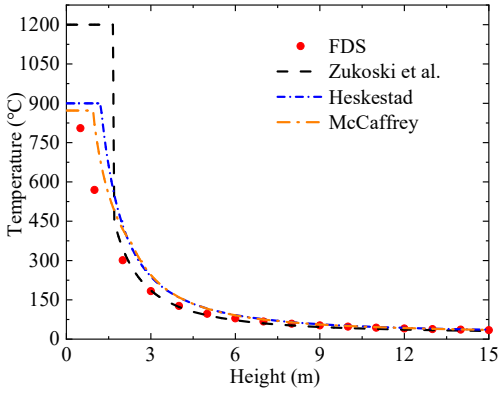

(n) Side length of 1 m – fire power of 500 kW/m^2

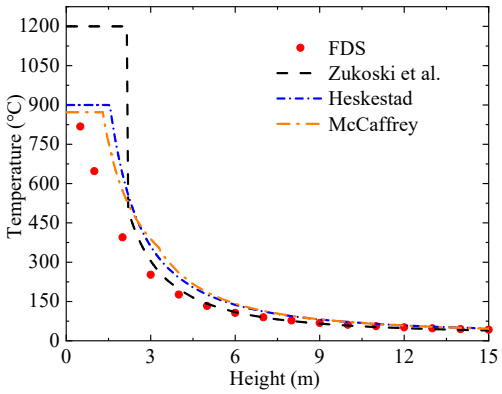

(o) Side length of 1.5 m – fire power of 500 kW/m^2

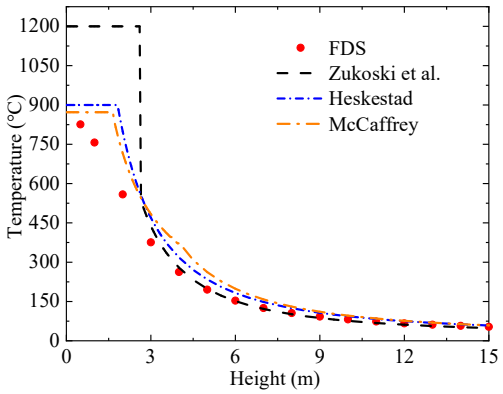

(p) Side length of 2 m – fire power of 500 kW/m^2

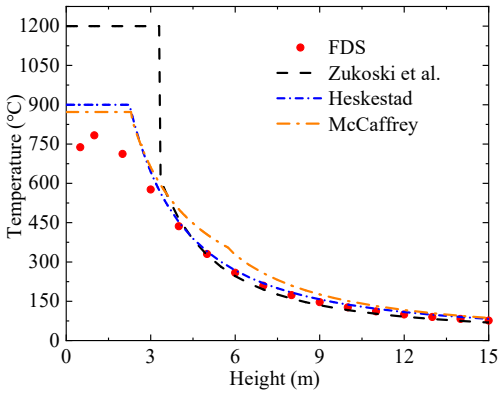

(q) Side length of 3 m – fire power of 500 kW/m^2

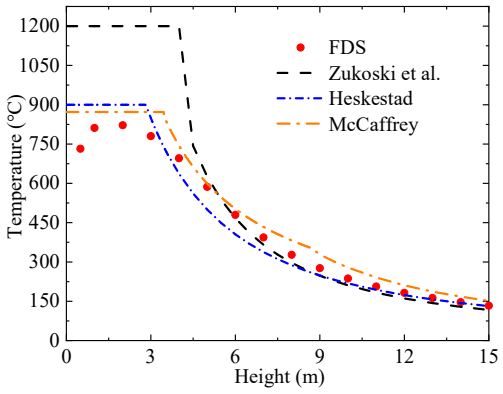

(r) Side length of 5 m – fire power of 500 kW/m^2

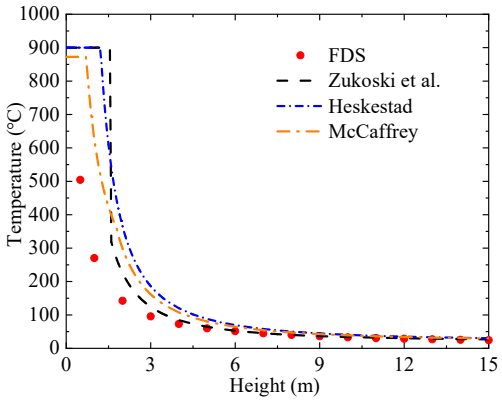

(s) Side length of 0.5 m – fire power of 1 MW/m^2

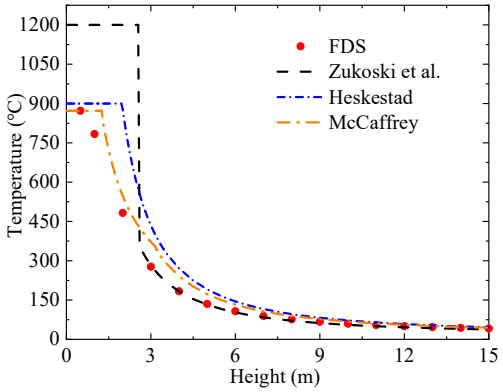

(t) Side length of 1 m – fire power of 1 MW/m^2

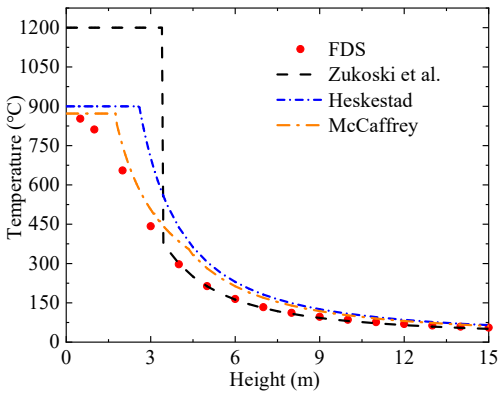

(u) Side length of 1.5 m – fire power of 1 MW/m^2

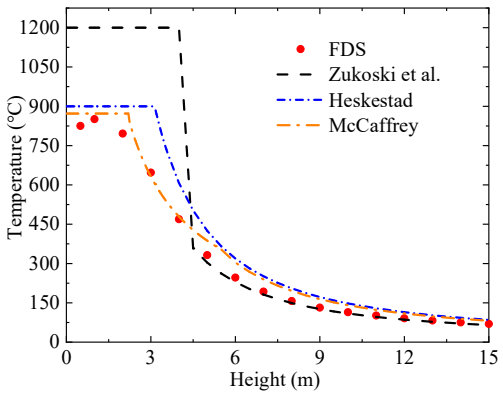

(v) Side length of 2 m – fire power of 1 MW/m^2

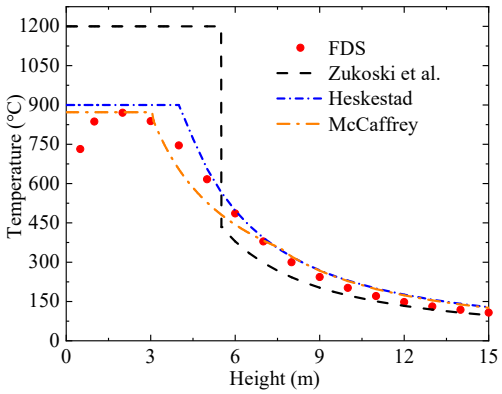

(w) Side length of 3 m – fire power of 1 MW/m^2

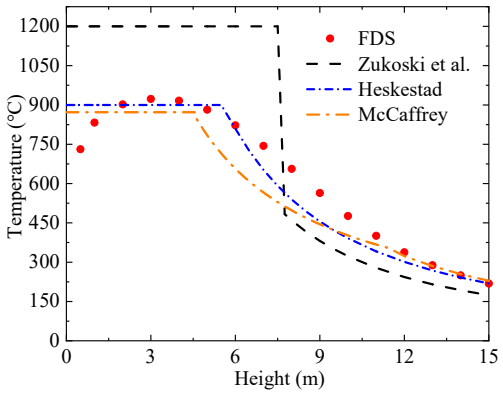

(x) Side length of 5 m – fire power of 1 MW/m^2

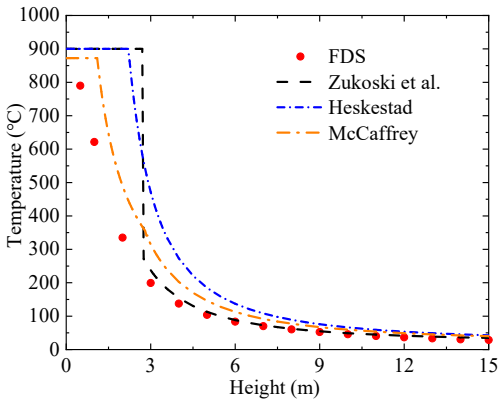

(y) Side length of 0.5 m – fire power of 3 MW/m^2

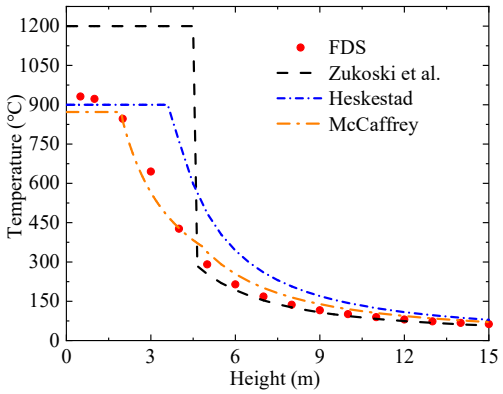

(z) Side length of 1 m – fire power of 3 MW/m^2

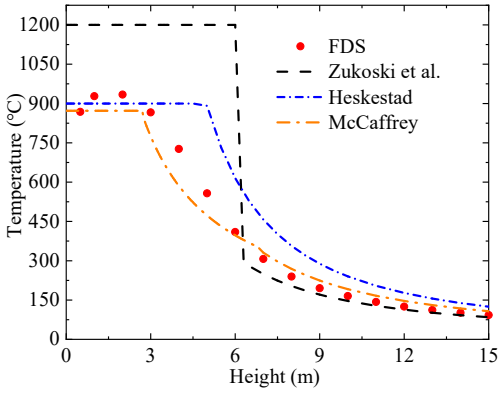

(aa) Side length of 1.5 m – fire power of 3 MW/m^2

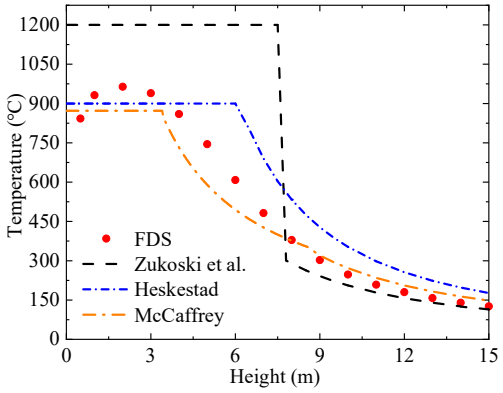

(ab) Side length of 2 m – fire power of 3 MW/m^2

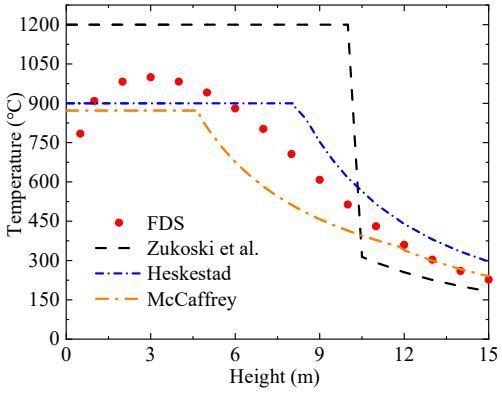

(ac) Side length of 3 m – fire power of 3 MW/m^2

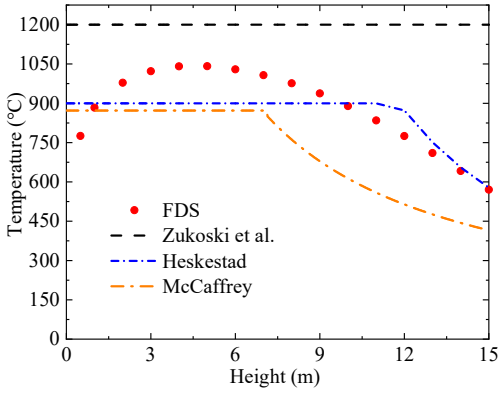

(ad) Side length of 5 m – fire power of 3 MW/m^2

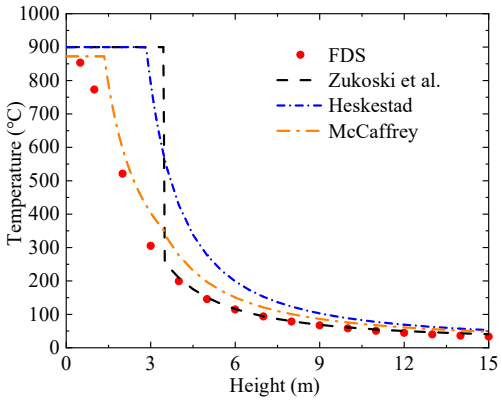

(ae) Side length of 0.5 m – fire power of 5 MW/m^2

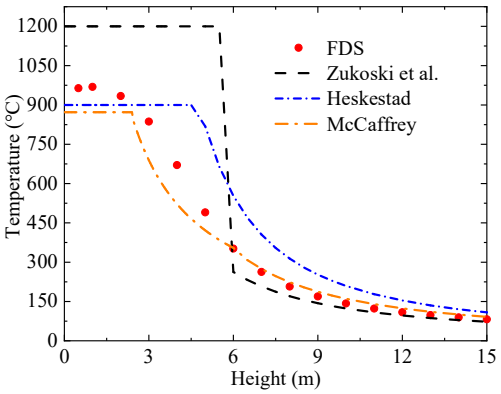

(af) Side length of 1 m – fire power of 5 MW/m^2

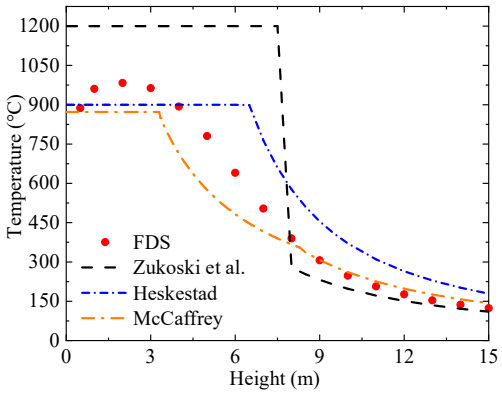

(ag) Side length of 1.5 m – fire power of 5 MW/m^2

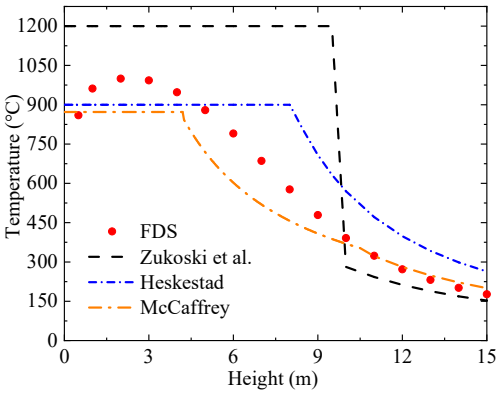

(ah) Side length of 2 m – fire power of 5 MW/m^2

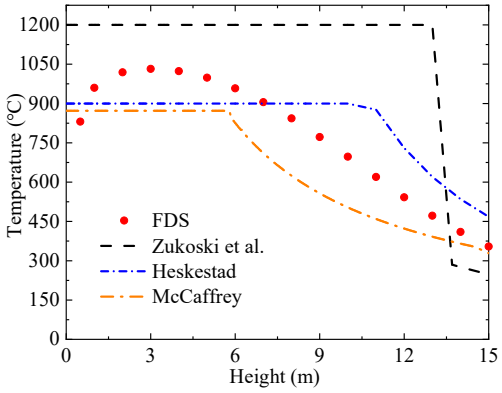

(ai) Side length of 3 m – fire power of 5 MW/m^2

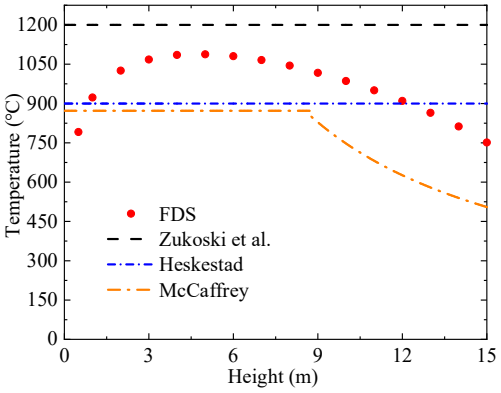

(aj) Side length of 5 m – fire power of 5 MW/m^2

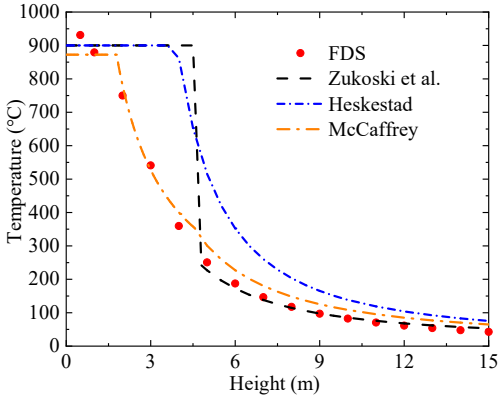

(ak) Side length of 0.5 m – fire power of 10 MW/m^2

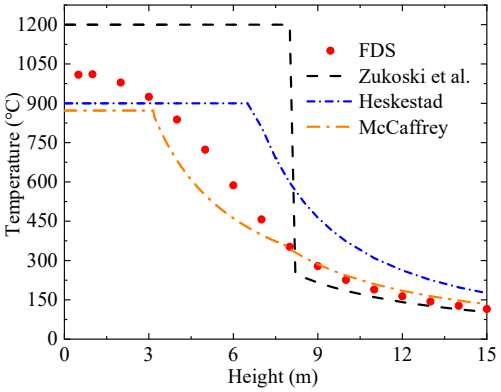

(al) Side length of 1 m – fire power of 10 MW/m^2

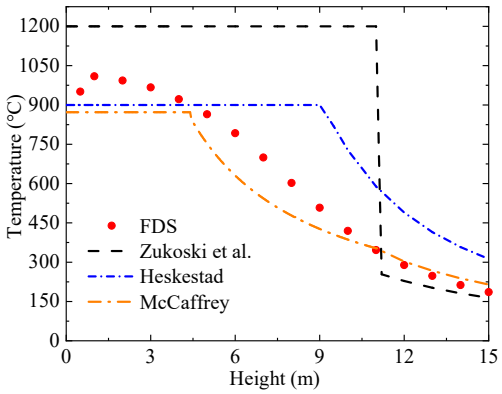

(am) Side length of 1.5 m – fire power of 10 MW/m^2

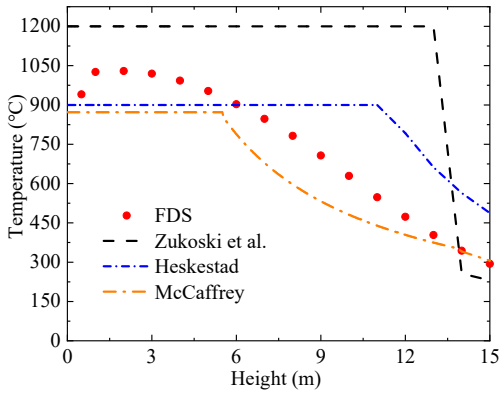

(an) Side length of 2 m – fire power of 10 MW/m^2

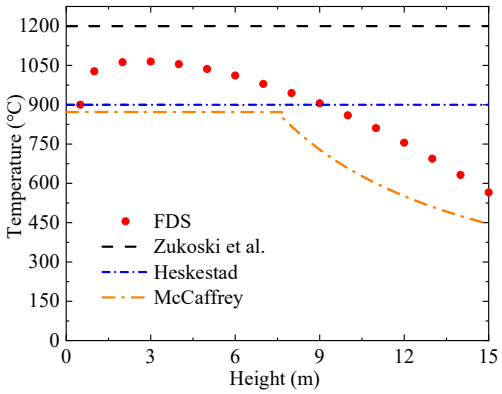

(ao) Side length of 3 m – fire power of 10 MW/m^2

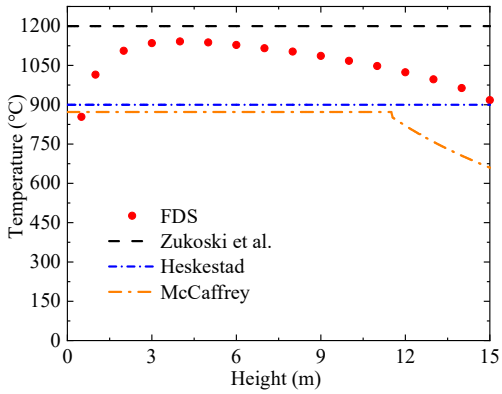

(ap) Side length of 5 m – fire power of 10 MW/m^2

References

[1] Y.W. Wu, S.G. Fan, B.B. He, et al. Research on the fire resistance design of high-strength steel hollow columns under axial compression. Engineering Structures, 2021, 234: 111943.

[2] Y.W. Wu. Experimental study and theoretical analysis on the fire resistance performance of large space stainless steel structures. PhD Thesis. School of Civil Engineering, Southeast University, Nanjing, 2024. (in Chinese)

[3] Peter23, "Beijing National Stadium," 2011. (Assessed September 2nd, 2024). https://zh.wikipedia.org/wiki/%E5%9B%BD%E5%AE%B6%E4%BD%93%E8%82%B2%E5%9C%BA_(%E5%8C%97%E4%BA%AC)#/media/File:Beijing_national_stadium.jpg

[4] London Stadium, "London Olympic Stadium," 2020. (Assessed September 2nd, 2024).

https://www.london-stadium.com/news/2020/july/stadium-seat-move-brings-fans-closer-to-the-action.html

[5] J.Q. Huang, G.Q. Li, Y. Du. The revision of two-zone fire model calculating the air temperature in large space buildings. Fire Science and Technology, 2005, 3: 279-283.

[6] C. Zhang, G.Q. Li. Simple formulae for calculating the gas temperature in large enclosure fire environment. Fire Safety Science, 2012, 21(2): 84-91.

[7] FIB. Task Group 4. 3, T. Luc. Fire Design of Concrete Structures: Structural Behaviour and Assessment: State-of-the-Art Report. Vol. 46, Fédération internationale du Béton (FIB), 2008.

[8] J.Y.R. Liew, L.K. Tang, Y.S. Choo. Advanced analysis for performance-based design of steel structures exposed to fires. Journal of Structural Engineering, 2022, 128(12): 1584-1593.

[9] A.H. Buchanan. Fire Engineering Design Guide. New Zealand, Centre for Advanced Engineering, University of Canterbury, 2001.

[10] P.H. Thomas, C.T. Webster, M.M. Raflery. Some experiments on buoyant diffusion flames. Combustion and Flame, 1961, 5: 359-367.

[11] B.J. McCaffrey. Purely buoyant diffusion flames: some experimental results. USA: NIST, 1979.

[12] E.E. Zukoski, T. Kubota, B. Cetegen. Entrainment in fire plumes. Fire Safety Journal, 1981, 3(3): 107-121.

[13] G. Heskestad. Virtual origins of fire plumes. Fire Safety Journal, 1983, 5(2): 174-185.

[14] G. Heskestad. Engineering relations for fire plumes. Fire Safety Journal, 1984, 7(1): 25-32.

[15] H.E. Morgan. Smoke control method in enclosed shopping complexes of one or more stories: a design summary. UK: BRE, 1979.

[16] S. Hiroomi, O. Sugawa, H. Kurioka, et al. Plume behavior in a confined tall and narrow space-as

396 one of sub-model of plume for an atrium fire. Fire Safety Science, 1994, 4: 551-562.
397 [17] W.H. Wu, G.Q. Zhu, G.Q. Zhang, et al. Research on natural filling of smoke in large space
398 buildings. China Fire Protection Association: Proceedings of the Science and Technology Annual
399 Conference of the China Fire Protection Association, 2011.
400 [18] G.W. Zhang, G.Q. Zhu, W.H. Wu, et al. Experimental study on the axial temperature of pool fire
401 plume centerline in tall and large spaces. Fire Science and Technology, 2012, 31(9): 907-909.
402 [19] E. Rackauskaite, M. Bonner, F. Restuccia, et al. Fire experiment inside a very large and open-plan
403 compartment: x-ONE. Fire Technology, 2022, 58: 905-939.
404 [20] W.K. Chow, W.M. Siu. Visualization of smoke movement in scale models of atrium. Joumal of
405 Applied Fire Science, 1993, 3(2): 93-111.
406 [21] Y. Du. A practical approach to fire resistance design of large space building grid structures. Ph.D.
407 thesis, Department of Structural Engineering, Tongji University, Shanghai, 2007. (in Chinese)
408 [22] E.F. Du. Experimental and theoretical research on the structural behavior of large space steel
409 structures subjected to natural fires. Ph.D. thesis, School of Civil Engineering, Southeast
410 University, Nanjing, 2016. (in Chinese)
411 [23] H. Nassiraei. Static strength of tubular T/Y-joints reinforced with collar plates at fire induced
412 elevated temperature. Marine Structures, 2019, 67: 102635.
413 [24] T. Tanaka, T. Yamana. Smoke control in large scale spaces, Part 1 and 2. Fire Science and
414 Technology, 1985, 5(1): 31-54.
415 [25] J. Stern-Gottfried, G. Rein. Travelling fires for structural design-Part I: Literature review. Fire
416 Safety Journal, 2012, 54: 74-85.
417 [26] J. Stern-Gottfried, G. Rein. Travelling fires for structural design-Part II: Design methodology. Fire

418 Safety Joumal, 2012, 54, 96-112.
419 [27] N. Tondini, C. Thauvoye, F. Hanus, et al. Development of an analytical model to predict the
420 radiative heat flux to a vertical element due to a localised fire. Fire Safety Journal, 2019, 105:
421 227-243.
422 [28] T. Chu, L. Jiang, G. Zhu, et al. Fire impact on vertical components subjected to a localised fire
423 estimated using a line source model. Fire Technology, 2023, 59: 2299-2331.
424 [29] Z. Zhu, S.E. Quiel, Near-field radiant heat flux from open-air gasoline and diesel pool fires:
425 Modified point source and discretized solid flame models. Fire Technology, 2021, 57: 1901-1926.
426 [30] R. Martínez-García, P. Jagadesh, O. Zaid, et al. The present state of the use of waste wood ash as
427 an eco-efficient construction material: A review. Materials, 2022, 15: 5349.
428 [31] A.İ. Çelik, Y.O. Özkılıç, Ö. Zeybek, et al. Mechanical behavior of crushed waste glass as
429 replacement of aggregates. Materials, 2022, 15: 8093.
430 [32] Y.W. Wu, S.G. Fan, L. Peng, et al. Scale test of large space stainless steel structure subjected to
431 natural fire. Journal of Constructional Steel Research, 2023, 210: 108059.
432 [33] N. Saliba, E. Real, L. Gardner. Shear design recommendations for stainless steel plate girders.
433 Engineering Structures, 2024, 59: 220-228.
434 [34] Y.T. Liang, O. Zhao, Y.L. Long, et al. Stainless steel channel sections under combined loading –
435 Part 1: Experimental study and numerical modelling. Journal of Constructional Steel Research, 2019,
436 152: 154-161.
437 [35] Y.T. Liang, T. Manninen, O. Zhao, et al. Elevated temperature material properties of a new high-
438 chromium austenitic stainless steel. Journal of Constructional Steel Research, 2019, 152: 261-273.
439 [36] M. Kucukler, Z. Xing, L. Gardner. Behaviour and design of stainless steel I-section columns in

fire. Journal of Constructional Steel Research, 2020: 165: 105890.

[37] O. Zhao, B. Rossi, L. Gardner, et al. Experimental and numerical studies of ferritic stainless steel cross-sections under combined compression and bending. Journal of Structural Engineering, 2016, 142(2): 04015110.

[38] A.V. Oppenheim, R.W. Schafer. Discrete–Time Signal Processing. USA: Prentice Hall, 2010.

[39] R.V. Hogg, J.W. McKean, A.T. Craig. Introduction to Mathematical Statistics. USA: Pearson, 2019.

[40] D.W. Scott. Multivariate Density Estimation: Theory, Practice, and Visualization. USA: John Wiley & Sons, 2015.

[41] MathWorks. MATLAB: The Language of Technical Computing. Natick, MA: MathWorks, 2023.

[42] K. McGrattan, S. Hostikka, R. McDermott, et al. Fire Dynamics Simulator User's Guide. USA: NIST Special Publication, 2013.

[43] M.J. Liu, S.J. Duan, Y.W. Wu, et al. Fire resistance design of austenitic SUS316 stainless columns subjected to axial compression. Journal of Constructional Steel Research, 2022, 198: 107540.

[44] Y.W. Wu, L. Peng, Y.J. Cui, et al. Mechanical properties of constructional PMMA at elevated temperatures and postfire conditions. Journal of Materials in Civil Engineering, 2023, 35(10): 04023377.

[45] Y.B. Huang, S.R. Lv. Building Fire Simulation Engineering Software: PyroSim from Beginner to Proficient. Beijing: Chemical Industry Press, 2017.

[46] G. Heskestad. Fire Plumes, Flame Height, and Air Entrainment. SFPE handbook of fire protection engineering: Third edition. Quincy, MA: National Fire Protection Association, 2002.

[47] CEN (European Committee for Standardization). prEN l991-1-2, Eurocode 1: Actions on structure

462 – Part 1-2: General actions – Actions on structures exposed to fire, 2021.

463 [48] T.G. Ma, J.G. Quintiere. Numerical simulation of axi-symmetric fire plumes: accuracy and

464 limitations. Fire Safety Journal, 2003, 38(5): 467-492.

465 [49] I. Goodfellow, Y. Bengio, A. Courville. Deep Learning. USA: MIT Press, 2016.